

Estimation of the liquid water saturation in PEM fuel cells: A low-power peaking-free dead-zone observer approach

Andreu Cecilia, Ramon Costa-Castelló

Abstract

Water management in polymer electrolyte membrane fuel cells (PEMFCs) is one of the most challenging issues affecting PEMFC efficiency and lifetime. The unavailability of reliably liquid water saturation sensors hinders the applicability of liquid water active control and supervision techniques. A promising technique that can be applied in this context are high-gain observers. However, the performance of this type of observer is significantly limited by the peaking phenomena and its noise sensibility. In general, this performance is not adequate for the considered estimation problem. For this reason, this work proposes a new high-gain observer without peaking and with reduced noise sensibility. The convergence of the observer is proven through rigorous arguments. Moreover, the algorithm is shown to be applicable in PEMFC systems through numerical simulations and experimental validation. It is shown that the proposed approach achieves at least a reduction of 32.3% of the mean square error in the estimation while maintaining the convergence rate and robustness of classical high-gain observers.

Keywords: PEM fuel cell, High-gain observer, Noise, Peaking Phenomena,

1. Introducción

In the current context of climate crisis, hydrogen has been established as a very promising element due to its high energy density, low to zero carbon emissions and zero production of particulates or nitrogen oxides. The deployment of hydrogen in the energy market requires developing and implementing hydrogen-based solutions in the transport sector and stationary back-up power generation field [1]. In these applications, an encouraging device are fuel cells. A hydrogen fuel cell is an electrochemical device that converts the chemical energy of hydrogen into direct current. Within all the different types of fuel cells, a remarkable one is the polymer electrolyte membrane fuel cell (PEMFC), by virtue of its high power density, low operating temperature and relatively easy construction.

PEMFCs consist of a solid polymer that is used as an electrolyte between the anode and the cathode. The fuel cell's anode is constantly delivered with pure hydrogen. This hydrogen is processed at a platinum based catalyst layer, which separates the H_2 into protons and electrons. The protons travel to the cathode catalyst layer through the membrane. However, due to the membrane ionic properties, the electrons are forced to travel through an external circuit, which generates the electrical load of the device. In parallel, the cathode is feed with pure oxygen or air, which flows to the cathode catalyst layer (CCL). In the CCL, the oxygen is combined with the protons

to generate water and heat, which closes the overall reaction. Figure 1 depicts a schematic of the PEM fuel cell operation.

Efficiency, reliability and life-time concerns hinders the implementation of PEMFCs in the energy market [2]. In the transport sector, variable vehicle operating conditions, as dynamic loads, starts-stops and idle speed, between others, accounts for the 50% of the fuel cell life-time reduction [3]. For this reason, optimal fuel cell operation requires the design of active control algorithms that can manage the internal variables during dynamic fuel cell operation.

A crucial topic in this manner is internal water management. Due to its proton conductivity and mechanical properties, the most used type of membrane is the perfluorosulfonic acid polymer membrane, being the most famous one the Nafion [4]. However, this type of membrane only presents acceptable proton conductivity under proper hydration [4]. As a consequence, if the membrane is drying out, the transport resistance is increased, which increases the ohmic resistance and accelerates membrane degradation [5]. External humidification is required in order to achieve adequate membrane hydration [6]. However, PEMFC humidifiers are characterized by slow dynamic response. Thus, external humidification can easily lead to excessive water accumulation due to the oxygen reduction reaction, which condenses in the cathode electrode. The presence of liquid water hinders the transport of oxygen through the electrode, which may lead to oxygen starvation and PEMFC degradation [7] [8].

As a consequence, optimal PEMFC operation requires developing active water management techniques that can avoid water accumulation. A useful variable to quantify the amount of water in the PEMFCs is the liquid water saturation in the porous media, s , [9] [10] [11] [12]. Liquid saturation is defined as the volume fraction in the pores, which is directly related with the membrane drying, oxygen starvation and channel flooding. Thus, an accurate monitoring of s is a key step in order to detect and prevent these adverse phenomena. Nevertheless, sensing the value of this variable is a conflictive topic. Direct visualizing/estimating techniques as the current distribution method [13], neutron radiography [14] or x-ray radiography [15], are far too expensive, slow and intrusive to be a viable option for the embedded feedback loops required in active water management. Non-intrusive methods as the pressure drop algorithm [16] [17] or external humidity sensors only retrieves information about the presence of liquid water in the channels, but cannot directly measure the water in the porous media.

Due to the absence of sensors, a natural approach is to implement a state observer. Initially, some authors studied the application of linear Luenberger observers [18] [19]. The resulting algorithms are simple and easy to implement, but are based on linearizing the dynamics of the fuel cell model, which results in a local solution to the problem. To overcome the local limitation, it is crucial to implement nonlinear observers. Following this line, other authors estimated the liquid water saturation through an unscented Kalman filter [20]. Theoretically, the resulting observer is not local, but its

convergence is difficult to prove and is sensitive to a correct modelling of the noise covariance. Alternatively, some authors studied the implementation of high-order sliding mode observers [21], which have shown to be insensitive to certain model uncertainty and give finite time convergence of the estimation error. Following the line of higher-order differentiators, another promising technique is the high-gain observer (HGO) [22]. This type of observer is robust to the same type of uncertainty which high-order sliding mode observers are insensitive. Moreover, the HGO is related to the semi-global separation principle [23], which allows not only to separate the observer design from the control one, but to recover the transient performance obtained from output feedback. This property is the base of powerful nonlinear control techniques as: output stabilization techniques [24], output regulation [25], and robust feedback-linearization methods [26], between others. These techniques can potentially improve the performance and robustness of active water management systems.

Nonetheless, HGO presents some drawbacks to be considered, that is, sensor noise sensibility and the peaking phenomena. Due to these drawbacks, in most cases, the HGO performance is not adequate for PEMFC systems, thus, this technique is usually discarded as a viable solution [27]. For this reason, this work proposes a new HGO scheme that can overcome the limitations of classic HGO. First, the peaking phenomena is eliminated by implementing a low-power peaking-free high-gain observer [28]. Second, the noise sensibility is reduced by introducing dynamic dead-zones in the observer cascade

structure [29][30].

The main contributions of this work can be summarized as follows.

- Propose a new observer that combines the low-power peaking-free architecture in [28] with the dynamic dead-zone filtering proposed in [29]. The new architecture eliminates the peaking phenomena of the classic HGO and reduces its noise sensitivity.
- Implement the proposed observer in a PEMFC model to estimate the liquid water saturation in the CCL from easy to measure signals.
- Compare the new observer with the classic HGO through a set of numerical simulations where sensor noise and initial conditions are considered.
- Validate the proposal in an experimental prototype considering an open-cathode PEM fuel cell.

The remaining of this paper is organized as follows: in section 2 the observer architecture is presented; section 3 presents the PEMFC model; section 4 implements the observer in the PEMFC model; section 5 validates the observer through a numerical simulation and shows the benefits over the classic HGO; section 6 validates the observer in a real experimental set-up; section 7 draws some conclusions.

2. Low-power peaking-free dead-zone observer

2.1. Classic high-gain observer

Let's consider a nonlinear single-output system in the so-called phase-variable form [31]

$$\begin{aligned}\dot{x}_i &= x_{i+1}, \quad i = 1, \dots, n-1 \\ \dot{x}_n &= \phi(\mathbf{x}, \mathbf{d}), \\ y &= x_1 + v\end{aligned}\tag{1}$$

where $\mathbf{x} = [x_1, \dots, x_n]^\top \in \mathbb{R}^n$ is the state, y is the measured output, $\mathbf{d} \in \mathbb{R}^q$ is any bounded unknown signal which may represent parametric uncertainties in the function $\phi(\cdot, \cdot)$ or unknown disturbances and v is unknown bounded high-frequency measurement noise. Moreover, it is assumed that $\mathbf{x} \in X$ and $\mathbf{d} \in D$, where X and D are compact sets of \mathbb{R}^n and \mathbb{R}^d , respectively. Finally, $\phi(\cdot, \cdot)$ is a known Lipschitz function with L_ϕ as the Lipschitz constant,

$$\|\phi(\boldsymbol{\xi}, \mathbf{d}) - \phi(\mathbf{z}, \mathbf{d})\| \leq L_\phi \|\boldsymbol{\xi} - \mathbf{z}\|.\tag{2}$$

Remark 2.1. *For simplicity, this section focuses in phase-variable forms, which is a common structure for mechanical and electrochemical systems. However, high-gain techniques can also be implemented to strict-feedback form systems [32], non-strict feedback form systems [31], general triangular forms [33] and systems which can be transformed to the previous mentioned*

forms by an appropriate coordinate change [34].

The classic high-gain observer for systems of the form (1) is a copy of the system plus an output estimation error injection term

$$\begin{aligned}\dot{\hat{\mathbf{x}}}_i &= \hat{\mathbf{x}}_{i+1} + \frac{\alpha_i}{\varepsilon^i}(\mathbf{y} - \hat{\mathbf{x}}_1), \quad i = 1, \dots, n-1 \\ \dot{\hat{\mathbf{x}}}_n &= \phi(\hat{\mathbf{x}}, 0) + \frac{\alpha_n}{\varepsilon^n}(\mathbf{y} - \hat{\mathbf{x}}_1)\end{aligned}\quad (3)$$

where $\hat{\mathbf{x}}$ is the estimation of the state \mathbf{x} , ε is the design high-gain parameter and $\alpha_1, \dots, \alpha_n$ are design parameters that are tuned so as the following polynomial

$$s^n + \alpha_1 s^{n-1} + \dots + \alpha_{n-1} s + \alpha_n \quad (4)$$

is Hurwitz.

Then, the high-gain's observer estimation error, $\mathbf{x} - \hat{\mathbf{x}}$, converges to a bounded region, provided that the design parameter ε is low enough (i.e. the gain factor $\frac{1}{\varepsilon}$ is high enough). This fact can be summarized in the following theorem.

Theorem 2.1. ¹[22] *Consider that the parameters α_i are such that (4) is Hurwitz. Then, there is a symmetric positive definite matrix \mathbf{P} solution of*

$$\mathbf{P}\mathbf{A}_{cl} + \mathbf{A}_{cl}^\top \mathbf{P} = -\mathbf{I} \quad (5)$$

¹The proof of all the theorems has been included as an appendix.

where

$$\mathbf{A}_{cl} = \begin{bmatrix} -\alpha_1 & 1 & 0 & \cdots & 0 \\ -\alpha_2 & 0 & 1 & \cdots & 0 \\ \vdots & \vdots & 0 & \ddots & \vdots \\ -\alpha_{n-1} & 0 & \cdots & & 1 \\ -\alpha_n & 0 & 0 & \cdots & 0 \end{bmatrix}.$$

Then, for all $\varepsilon \leq \min\{\frac{1}{2L_\phi\|\mathbf{P}\|}, 1\}$, the estimation error of the observer (3) satisfies the following bound for all $t > 0$

$$|x_i - \hat{x}_i| \leq \frac{k_1}{\varepsilon^{i-1}} e^{-\frac{k_2}{\varepsilon}t} |x_i(0) - \hat{x}_i(0)| + \varepsilon^{n+1-i} k_2 M + \frac{k_4}{\varepsilon^{i-1}} \|v\|_\infty, \quad i = 1, \dots, n \quad (6)$$

where k_1, \dots, k_4 are some positive constants, M is a positive constant proportional to $\|\phi(\mathbf{x}, \mathbf{d}) - \phi(\mathbf{x}, 0)\|$ and $\|\cdot\|_\infty$ is the maximum value of the norm.

By direct inspection of the estimation error bound (6) it is possible to highlight the main benefits and potential drawbacks of high-gain observation.

On the one hand, the first term, $\frac{k_1}{\varepsilon^{i-1}} e^{-\frac{k_2}{\varepsilon}t} |x_i(0) - \hat{x}_i(0)|$, converges to zero with a rate proportional to $\frac{1}{\varepsilon}$. Therefore, in the absence of noise and uncertainty (i.e. $M = \|v\|_\infty = 0$), the estimation error converges to zero and its rate of convergence can be made arbitrary fast by decreasing ε . The second term, $\varepsilon^{n+1-i} k_2 M$, depicts the effect of unknown disturbances or uncertainty in the estimation error. Roughly speaking, in the absence of measurement noise (i.e. $M \neq 0, \|v\|_\infty = 0$) the estimation error converges to a bounded

region proportional to the amount of model uncertainty, which can be arbitrary reduced by decreasing the design parameter ε . It is possible to see that the high-gain observer can be made arbitrary fast and robust by just decreasing a singular design parameter, ε .

On the other hand, it should be noticed that the first term is multiplied by a factor $\frac{1}{\varepsilon^{i-1}}$, which does not alter the decay rate of the term, but significantly increases its value at initial time instants. As a consequence, the observer's states "peaks" during the transient, and the amplitude of this peak is increased as the design parameter ε is decreased. Therefore, the smaller is the desired observer decay rate, the larger the peaking will be. This abrupt increase/decrease of the observer's states, known as the peaking phenomena, can have disastrous effects on the observer application, and has to be dealt with caution. Finally, the third element of (6), $\frac{k_4}{\varepsilon^{i-1}}\|v\|_\infty$, depicts that, in the absence of uncertainty or unknown disturbances (i.e. $M = 0$), the estimation error converges to a bounded region proportional to the noise supremum norm, $\|v\|_\infty$. Notice that the bound of this region is also proportional to $\frac{1}{\varepsilon^{i-1}}$. As a consequence, in the presence of noise, the accuracy of the observer is significantly deteriorated as the design parameter ε is decreased.

As a summary, there is a clear trade-off during the design of a HGO. The appealing property of fast and robust estimation, that is achieved by decreasing the parameter ε , comes with an increase of the peaking phenomena and an increase of the observer's measurement noise sensibility. This trade-off limits the viable robustness and convergence rate of the observer. Therefore,

with the aim of improving the performance of the HGO, next subsections will focus on eliminating the peaking phenomena and reducing the noise sensibility.

2.2. Peaking Phenomena Reduction: Low-power Peaking-free Observer

Different schemes can be found in the literature in order to address the peaking phenomena. The initial efforts focused on modifying the observer dynamics in order to bound its states to a prescribed set. Some notable examples are the use of projection algorithms [35], the implementation of hybrid instantaneous jumps [36] or modify the observer under some convexity assumptions [37]. Although the presented results reduced the peaking phenomena, the high-gain observer's dynamics were significantly modified and its implementation in feedback loops was not trivial. Another strategy was based on interconnecting a cascade of reduced high-gain observers of order 1 and including saturations between cascaded observers [38]. It was a promising result, as a similar strategy, without feedback interconnection, was shown to be applicable in output feedback control [39]. However, the estimation error was only proven to converge to a bounded region. The extension of these results lead to the creation of the low-power peaking-free observer [28]. This new observer structure presented the outstanding results of eliminating the peaking phenomena in all its states, improving the observer's sensibility to noise and preserving the classic high-gain performance. This subsection will focus on presenting the design highlights of the low-power peaking-free

observer. It should be remarked that the results presented in this subsection are just a brief summary of the results already presented in [28].

The low-power peaking-free observer scheme is based on interconnecting $n-1$ blocks of dimension 2, characterized by the states (\hat{x}_i, η_i) , which provides an estimation of (x_i, x_{i+1}) , $i = 1, \dots, n-1$, respectively. The $n-1$ second order systems are connected with a one dimensional block which provides an estimation of x_n . The observer includes $n-1$ "virtual states", η_i , $i = 2, \dots, n-1$, which provide a redundant estimation of x_i , $i = 2, \dots, n$. The peaking-free idea is to saturate the virtual states, $\boldsymbol{\eta}$, in a way that the state estimation error, $\mathbf{x} - \hat{\mathbf{x}}$, is continuous, differentiable and is upper bounded by a constant independent of ε . Specifically, for phase-variable systems (1), the observer takes the following form

$$\begin{aligned}\dot{\hat{x}}_i &= \eta_i + \frac{\alpha_i}{\varepsilon} \mathbf{e}_i, \quad i = 1, \dots, n-1 \\ \dot{\hat{x}}_n &= \phi(\hat{\mathbf{x}}, 0) + \frac{\alpha_n}{\varepsilon} \mathbf{e}_n \\ \dot{\eta}_i &= \text{sat}_{r_{i+2}}(\eta_{i+1}) + \frac{\beta_i}{\varepsilon^2} \mathbf{e}_i, \quad i = 1, \dots, n-2 \\ \dot{\eta}_{n-1} &= \phi(\hat{\mathbf{x}}, 0) + \frac{\beta_{n-1}}{\varepsilon^2} \mathbf{e}_{n-1}\end{aligned}\tag{7}$$

with

$$\begin{aligned}\mathbf{e}_1 &\triangleq y - \hat{x}_1, \\ \mathbf{e}_i &\triangleq \text{sat}_{r_i}(\eta_{i-1}) - \hat{x}_i, \quad i = 2, \dots, n\end{aligned}$$

where $\hat{\mathbf{x}} = [\hat{x}_1, \dots, \hat{x}_n]^\top \in \mathbb{R}^n$ is the estimation of \mathbf{x} , $\boldsymbol{\eta} = [\eta_1, \dots, \eta_{n-1}]^\top \in \mathbb{R}^{n-1}$ is the virtual state, $\boldsymbol{\alpha} = [\alpha_1, \dots, \alpha_n]^\top \in \mathbb{R}^n$ and $\boldsymbol{\beta} = [\beta_1, \dots, \beta_n]^\top \in \mathbb{R}^{n-1}$ are positive design parameters, ε is the design high-gain parameter and $\text{sat}_k(\cdot)$ is a saturation function to be designed which satisfies

$$\text{sat}_k(s) = s \quad \forall |s| \leq k, \quad \text{sat}_k(s) = k \quad \forall |s| \geq k. \quad (8)$$

To ease the understanding of equation (7), it is convenient to implement the observer in a simple example.

Example: Consider a second order system, i.e. $n = 2$, in phase-variable form (1). Then, the observer in (7) would take the following form:

$$\begin{aligned} \dot{\hat{x}}_1 &= \eta_1 + \frac{\alpha_1}{\varepsilon} \mathbf{e}_1, \\ \dot{\hat{x}}_2 &= \phi(\hat{\mathbf{x}}, 0) + \frac{\alpha_2}{\varepsilon} \mathbf{e}_2 \\ \dot{\eta}_1 &= \phi(\hat{\mathbf{x}}, 0) + \frac{\beta_1}{\varepsilon^2} \mathbf{e}_1. \end{aligned}$$

□

The parameter design in this new observer is more convoluted than in the classical high-gain observer and requires the definition of some extra matrices [28]. Define the following

$$\mathbf{B}_k \triangleq \begin{bmatrix} 0_{i-k,1} \\ 1 \end{bmatrix} \in \mathbb{R}^{i \times 1} \quad \forall k \in \mathbb{N}, \quad \mathbf{E}_i \triangleq \begin{bmatrix} -\alpha_i & 0 \\ -\beta_i & 0 \end{bmatrix} \in \mathbb{R}^{2i \times 2i}, \quad i = 1, \dots, n-1.$$

Next, let $\mathbf{M}_n \in \mathbb{R}^{(2n-1) \times (2n-1)}$ be a matrix recursively constructed as follows

$$\begin{aligned} \mathbf{M}_1 &\triangleq \mathbf{E}_1, \\ \mathbf{M}_i &\triangleq \begin{bmatrix} \mathbf{M}_{i-1} & \mathbf{B}_{2(i-1)}\mathbf{B}_2^\top \\ \begin{bmatrix} \alpha_i \\ \beta_i \end{bmatrix} \mathbf{B}_{2(i-1)}^\top & \mathbf{E}_i \end{bmatrix} \quad i = 2, \dots, n-1, \\ \mathbf{M}_n &\triangleq \begin{bmatrix} \mathbf{M}_{n-1} & 0 \\ \alpha_n \mathbf{B}_{2(i-1)}^\top & -\alpha_n \end{bmatrix}. \end{aligned}$$

Finally, let $\mathbf{\Lambda}_i(s) : [0, 1] \rightarrow \mathbb{R}^{2i \times 2i}$, $i = 1, \dots, n$ be a continuous matrices defined as

$$\begin{aligned} \mathbf{\Lambda}_1(s) &\triangleq \mathbf{M}_1, \\ \mathbf{\Lambda}_i(s) &\triangleq \begin{bmatrix} \mathbf{M}_{i-1} & s\mathbf{B}_{2(i-1)}\mathbf{B}_2^\top \\ \begin{bmatrix} \alpha_i \\ \beta_i \end{bmatrix} \mathbf{B}_{2(i-1)}^\top & \mathbf{E}_i \end{bmatrix} \quad i = 2, \dots, n-1, \\ \mathbf{\Lambda}_n(s) &\triangleq \mathbf{M}_n \end{aligned}$$

Now, after defining these matrices, it is possible to summarize the low-power peaking-free observer design and performance properties in the following theorem.

Theorem 2.2. [28] *Design r_i of the saturation functions as $r_i \triangleq \max_{\mathbf{x} \in X} |x_i|$ for $i = 1, \dots, n$. Moreover design $\alpha_i, i = 1, \dots, n$ and $\beta_i, i = 1, \dots, n-1$ such that there*

exists $\mathbf{P}_i = \mathbf{P}_i^\top > 0$ and $\mu_i > 0$ that satisfy the following [28]:

$$\mathbf{P}_i \mathbf{\Lambda}_i(s) + \mathbf{\Lambda}_i(s)^\top \mathbf{P}_i \leq \mu_i \mathbf{I} \quad \text{for } i = 1, \dots, n, \quad \forall s \in [0, 1]. \quad (9)$$

Then, provided that $\|\mathbf{v}\|_\infty$ is small enough, there exists a value ε^* such that for all $\varepsilon \leq \min\{\varepsilon^*, 1\}$ the estimation error of the observer (7) satisfies the following bound

$$|\mathbf{x}_i - \hat{\mathbf{x}}_i| \leq \min\left\{\frac{\mathbf{k}_1}{\varepsilon^{i-1}} e^{-\frac{\mathbf{k}_2}{\varepsilon} t} |\mathbf{x}_i(0) - \hat{\mathbf{x}}_i(0)| + \varepsilon^{n+1-i} \mathbf{k}_2 M + \frac{\mathbf{k}_4}{\varepsilon^{i-1}} \|\mathbf{v}\|_\infty, \bar{\mathbf{p}}_i\right\} \quad (10)$$

where $\mathbf{k}_1, \dots, \mathbf{k}_4$ are some positive constants (different from the ones in (6)) and $\bar{\mathbf{p}}_i$ is a positive constant independent from ε .

Remark 2.2. Condition (9) may seem very restrictive and convoluted to compute. However, it is always possible to find some parameters α_i and β_i that makes the matrix inequality feasible. Moreover, a methodology to design α_i and β_i is presented in [40].

The benefits of this observer structure can be seen by direct comparison of the bound (6) with the bound (10). First, in the absence of noise and uncertainty (i.e. $\mathbf{d} = \|\mathbf{v}\|_\infty = 0$), the estimation error converges to zero with a decay rate proportional to $\frac{1}{\varepsilon}$. In the presence of uncertainty, the estimation error converges to a bounded region that can be made arbitrary small by reducing ε . Therefore, the observer maintains the decay rate and robustness performance of the classic high-gain observer.

Second, by inspection of (10), it is possible to see that

$$\|x_i - \hat{x}_i\| \leq \bar{p}_i, \quad i = 1, \dots, n$$

where \bar{p}_i is independent from ε .

Thus, decreasing ε does not induce any peak in the observer's states and the peaking phenomena of the classic high-gain observer is practically solved.

Nevertheless, the noise sensibility conflict of high-gain observation has not been addressed. Although, the extra states, $\boldsymbol{\eta}$, of the low-power peaking-free observer act as low pass filters and reduces the noise sensibility of the system [28], the measurement noise still propagates through the observer and gets multiplied by a factor $\frac{1}{\varepsilon^{i-1}}$ in the estimation error bound (10). Moreover, if too much noise is present in the measured output, the virtual states, η_i , will enter and never exit the saturation function, $\text{sat}_{r_i}(\cdot)$, which breaks the observer's convergence proof [28]. For this reason, the next section will focus on introducing some tools that can be used to reduce the noise sensibility of the observer without degrading the observer performance. Moreover, a novel observer will be presented.

2.3. Noise Sensibility Reduction: Dynamic dead-zone filtering

In general, measurement noise is limited to the high-frequency spectrum. For this reason, it is common to apply a low-pass filter that filters out the high-frequency components of the measured output. However, the effectiveness of the filter relies on increasing its time constant, which significantly

slows down the estimation of the observer or, in the worst case, makes the observer lose its exponential convergence [41]. For this reason, some authors have focused on alternative ways of reducing the noise sensibility.

In recent years, some authors have studied the use of nonlinear dynamical filters with the aim of maintaining the filtering capabilities of low-pass filters without deteriorating the observer performance. A promising result is the use of dynamic dead-zones in the output-injection term [29][30][42][43]. The idea is to substitute the term $y - \hat{x}_1$ of (3) or (7) by a “deadzoned” version, $\text{dz}_{\sqrt{\sigma}}(y - \hat{x}_1)$, where $\text{dz}_{\sqrt{\sigma}}(\cdot)$ is the dead-zone function computed as

$$\text{dz}_{\sqrt{\sigma}}(a) = a - \text{sat}_{\sqrt{\sigma}}(a), \quad (11)$$

where the factor $\sqrt{\sigma}$ is the dead-zone amplitude (see Figure 2 for an example of different dead-zone functions with different amplitudes).

The motivation behind this modification is that the dead-zone function is capable of eliminating part of the persistent sensor noise. Notice that the observer’s error dynamics runs in open-loop around zero, which may destabilize the observer. For this reason, the dead-zone amplitude, $\sqrt{\sigma}$, is dynamically adapted to the amount of noise. By applying this modification, in the absence of measurement noise, the observer maintains asymptotic convergence to zero, and, in the presence of noise, the observer converges to an ultimate bound lower than its original non-dead-zone version.

This section proposes combining the low-power peaking-free observer (7)

with the dynamic dead-zone strategy, in order to reduce the noise introduced to the observer and its propagation through the cascade structure. Specifically, for phase-variable systems (1), the observer takes the following form

$$\dot{\hat{\mathbf{x}}}_i = \eta_i + \frac{\alpha_i}{\varepsilon} \text{dz}_{\sqrt{\sigma_i}}(\mathbf{e}_i), \quad i = 1, \dots, n-1 \quad (12)$$

$$\dot{\hat{\mathbf{x}}}_n = \phi(\hat{\mathbf{x}}, 0) + \frac{\alpha_n}{\varepsilon} \text{dz}_{\sqrt{\sigma_n}}(\mathbf{e}_n)$$

$$\dot{\eta}_i = \text{sat}_{r_{i+2}}(\eta_{i+1}) + \frac{\beta_i}{\varepsilon^2} \text{dz}_{\sqrt{\sigma_i}}(\mathbf{e}_i), \quad i = 1, \dots, n-2$$

$$\dot{\eta}_{n-1} = \phi(\hat{\mathbf{x}}, 0) + \frac{\beta_{n-1}}{\varepsilon^2} \text{dz}_{\sqrt{\sigma_{n-1}}}(\mathbf{e}_{n-1})$$

$$\dot{\sigma}_i = -\frac{q_i}{\varepsilon^2} \sigma_i + p_i \varepsilon \|\mathbf{e}_i\|, \quad i = 1, \dots, n \quad (13)$$

with

$$\mathbf{e}_1 \triangleq y - \hat{\mathbf{x}}_1,$$

$$\mathbf{e}_i \triangleq \text{sat}_{r_i}(\eta_{i-1}) - \hat{\mathbf{x}}_i, \quad i = 2, \dots, n$$

where $\text{dz}_{\sqrt{\sigma_i}}(\cdot)$ is the dynamic dead-zone defined in (11), $\sqrt{\sigma}$ is the amplitude of the dead-zone, q_i and p_i are some positive design parameters. The rest of parameters are introduced in (7).

This observer is the same as (7) but, the error signals $\mathbf{e}_1, \mathbf{e}_2, \dots, \mathbf{e}_n$ are filtered through dynamic dead-zones. The amplitude of the dead-zones are modified according to the dynamics of (13).

Theorem 2.3. *Consider the low-power peaking-free observer with dynamic*

dead-zone modification (12) and assume that α_i and β_i for $i = 1, \dots, n$ satisfy (9). Then, for a fixed $p_i > 0$ for $i = 1, \dots, n$ there exist some values $\varepsilon^* > 0$ and $q^* > 0$ such that, for $\varepsilon < \varepsilon^*$ and $q_i > q^*$ for $i = 1, \dots, n$, the observer estimation error, $x_i - \hat{x}_i$, converges to an ultimate bound proportional to $\frac{1}{\varepsilon^{i-1}} \|v\|_\infty$, provided that $\|v\|_\infty$ is small enough.

Remark 2.3. *The amount of noise that is introduced and propagated through the observer is significantly reduced by the dead-zone modification. However, the estimation error's ultimate bound remains proportional to $\frac{1}{\varepsilon^{i-1}}$. Therefore, the observer high-gain parameter, ε , still has to be designed with caution.*

Remark 2.4. *The idea of combining dynamic dead-zones with low-power observers was proposed in [30], with some major differences. First, the observer does not include saturation functions. Therefore, it is sensible to the peaking phenomena. Second, it only applies the dynamic dead-zone to the signal e_1 . As a consequence, the dead-zone modification only reduces the amount of noise that enters the observer, but not the one that propagates through the cascade structure.*

3. Open-cathode PEM Fuel Cell Model

This work will focus on a lumped parameter model developed by Strahl et. al. [44], which has demonstrated to be descriptive enough for fuel cell control design [45]. The model depicts the behaviour of the fuel cell through 3 sub-models: a thermal sub-model, a liquid water transport sub-model and an electrochemical sub-model.

Relative to the thermal sub-model, the system is considered to have a uniform temperature T_{fc} , the dynamics of which are depicted by

$$\dot{T}_{fc} = K_1(1.48n_{cell} - V_{fc})I + K_2(T_{amb} - T_{fc})v_{air},$$

where n_{cell} is the number of cells in the stack, V_{fc} is the fuel cell stack voltage, I is the exchange current, T_{amb} is the ambient temperature, v_{air} is the cathode air velocity, K_1 and K_2 are some parameters computed as

$$K_1 = \frac{1}{m_{fc}C_{p,fc}}, \quad K_2 = \frac{\rho_{air}A_{inlet}C_{p,air}}{m_{fc}C_{p,fc}}$$

where m_{fc} is the stack's mass, $C_{p,fc}$ is the specific heat capacity, ρ_{air} is the air density, A_{inlet} is the inlet cross-sectional area, $C_{p,air}$ is the air heat capacity.

The dynamics of the liquid water saturation, s , are characterized through the following expression

$$\dot{s} = \frac{1}{K_s}(K_3I - K_4(p^0 e^{-E_a/(k_b T_{fc})} - p_v)s) - K_5 s^4(1.42 - 4.24s + 3.79s^2)$$

where K_s is the liquid water accumulation coefficient, p^0 is a pre-exponential factor, k_B is the Boltzmann's constant and E_a is the activation energy of the evaporation process.

The parameters K_3 , K_4 and K_5 are computed as

$$K_3 = \frac{1}{2FA_{geo}M_{H_2O}}, \quad K_4 = K_{evap} \frac{M_{H_2O}}{RT_{fc}A_{pore}}, \quad K_5 = \sigma_w \cos \Theta \sqrt{\epsilon_{eff} K_{eff}} \frac{\rho_l}{K_s \mu_l}$$

where F is the Faraday's constant, A_{geo} is the CCL's surface area, M_{H_2O} is the water molar mass, K_{evap} is the evaporation time constant, A_{pore} is the pore surface per unit volume, R is the ideal gas constant, σ_w is water's surface tension, Θ is the effective contact angle in the diffusive media, ϵ_{eff} is the CCL's effective porosity, K_{eff} is the CCL's effective permeability, ρ_l is the water density, μ_l is the liquid water viscosity.

Finally, the model includes a static relation between the fuel cell stack temperature, T_{fc} , liquid water saturation, s , and the stack voltage, V_{fc} ,

$$V_{fc} = n_{cell} \left(E_{th} - \frac{RT_{fc}}{n\alpha F} \ln \left(\frac{j}{j_0} \right) - R_{ohm} I \right) \quad (14)$$

where E_{th} the theoretical potential obtained through the Nernst equation [46], j is the exchange current density, α is the transfer coefficient, n is the number of electrons transferred in the reaction, R_{ohm} accounts for the ionic conductivity of the membrane and the resistance of the fuel cell's electric conductive components and j_0 is the reference exchange current density which computed as

$$j_0 = 0.21 j_0^{ref} a_c \left(1 - \left(\frac{s_{opt} - s}{s_{opt}} \right)^{1/3} \right) e^{(-\Delta G^*/(RT_{fc})(1-(T_{fc}/T_{ref})))}$$

where j_0^{ref} , a_c and T_{ref} are the reference exchange current, electrode rugosity and stack temperature, respectively, at a reference operating conditions; ΔG^* is the activation energy of the oxygen reduction reaction and s_{opt} is the liquid water saturation in which the effective electrochemical active area is

maximum.

The value of all the model parameters and constants is included in Appendix Appendix D.

In order to ease the read of the following sections, the PEMFC model will be rewritten in the following state-space form

$$\dot{\mathbf{x}} = \mathbf{f}_s(\mathbf{x}, I) + \mathbf{g}(\mathbf{x})v_{air}. \quad (15)$$

The state vector \mathbf{x} , is,

$$\mathbf{x} = \begin{bmatrix} T_{fc} \\ s \end{bmatrix}$$

and \mathbf{f}_s , \mathbf{g} are,

$$\mathbf{f}_s(\mathbf{x}, I) = \begin{bmatrix} K_1(1.48n_{cell} - V_{fc}(\mathbf{x}))I \\ \frac{1}{K_s}(K_3I - K_4f_p(x_1)x_2) - K_5f_d(x_2) \end{bmatrix}$$

$$\mathbf{g}(\mathbf{x}) = \begin{bmatrix} K_2(T_{amb} - x_1) \\ 0 \end{bmatrix}$$

Finally, the measured output of the system, y , is the fuel cell stack temperature, $y = x_1 = T_{fc}$.

4. Main result

In this section, the low-power peaking-free observer with dynamic dead-zone filtering will be implemented in the PEMFC model.

4.1. Observability analysis

Nonlinear systems do not have a unified observability analysis and multiple observability assumptions can be taken into account depending on the observer to be designed [33]. In this section we are going to focus on the observability rank condition [47]. The observability rank test is a nonlinear extension of the Kalman rank condition, and shows if it is possible to reconstruct the system states through the knowledge of the measured output, input and a finite number of its derivatives. The observability rank condition, under some structural assumptions, is a sufficient condition for the existence of a high-gain observer.

Definition 4.1. *Consider a generic nonlinear system*

$$\dot{\mathbf{x}} = \mathbf{f}(\mathbf{x}, \mathbf{u}) \quad (16)$$

$$y = \mathbf{h}(\mathbf{x}) \quad (17)$$

where $\mathbf{x} \in \mathbb{R}^n$ is the state vector, $\mathbf{u} \in \mathbb{R}^q$ the input vector and $y \in \mathbb{R}$ is the output vector. Moreover, $\mathbf{f} \in \mathbb{R}^{n \times (n+q)}$ and $\mathbf{h} \in \mathbb{R}$ are vector functions, potentially nonlinear.

Let the observability map of order k of a generic nonlinear system be defined as

$$\mathbf{O}_k = \begin{bmatrix} y \\ \dot{y} \\ \vdots \\ y^{(k)} \end{bmatrix}. \quad (18)$$

Then, system (16) is rank observable of order k if the following holds

$$\text{rank} \left(\frac{\partial \mathbf{O}_k}{\partial \mathbf{x}} \right) = n. \quad (19)$$

Let's study the rank condition in the concerned PEMFC model. Consider the observability map of order 2 for system (15),

$$\mathbf{O}_2 = \begin{bmatrix} y \\ \dot{y} \end{bmatrix} = \begin{bmatrix} T_{fc} \\ K_1(E_{thn_{cell}} - V_{fc})I + K_2(T_{amb} - T_{fc})v_{air} \end{bmatrix}$$

The Jacobian of the observability map satisfies

$$\frac{\partial \mathbf{O}_2}{\partial \mathbf{x}} = \begin{bmatrix} 1 & 0 \\ \frac{\partial L_{f_s} T_{fc}}{\partial T_{fc}}(\mathbf{x}) - K_2 v_{air} & \frac{\partial L_{f_s} T_{fc}}{\partial s}(\mathbf{x}) \end{bmatrix} \quad (20)$$

where

$$\begin{aligned}\frac{\partial L_{f_s} T_{fc}}{\partial T_{fc}}(\mathbf{x}) &= -K_1 \frac{R}{n\alpha F} I \left(\frac{\Delta G^*}{RT_{fc}} - \ln \left(\frac{I}{A_{geo} j_0} \right) \right) \\ \frac{\partial L_{f_s} T_{fc}}{\partial s}(\mathbf{x}) &= \frac{-K_1 RT_{fc} I}{3n\alpha F \left(1 - \left(\frac{s_{opt} - s}{s_{opt}} \right)^{1/3} \right) \left(\frac{s_{opt} - s}{s_{opt}} \right)^{2/3} s_{opt}}\end{aligned}$$

The Jacobian (20) is full rank in the domain

$$D = \{T_{fc}, s, I \in \mathbb{R} : T_{fc} \neq 0; 0 < s < s_{opt}; I \neq 0\} \quad (21)$$

The operating conditions $T_{fc} = 0$, $s = 0$ and/or $s = s_{opt}$ are physically impossible. Moreover, during normal operation of the fuel cell, the current is always greater than zero. Therefore, the Jacobian (20) is full rank in all the valid operating conditions of the fuel cell and the system is rank observable [47] independently of the input.

From this result, one can extract two conclusions. First, the unknown states can be uniquely expressed as a function of y, \dot{y}, I . Second, the system is observable for any input, v_{air} , i.e., is uniformly observable in the air velocity.

Remark 4.1. *Even though the values $s = 0$ and $s = s_{opt}$ are physically unreachable, if the observer estimation peaks excessively during the transient, the observer's states may reach these values, making the system unobservable. For this reason, it is crucial to minimize the peaking phenomena of the observer or eliminate it through a peaking-free structure.*

4.2. System Transformation

The low-power peaking-free observer can only be implemented in phase variable forms or similar triangular structures [33]. The studied fuel cell system (15) does not present a triangular structure, thus, the observer cannot be implemented directly on the system. However, it is possible to transform the system to a triangular structure through an appropriate coordinate change [34]. From the past observability analysis, it was concluded that the system is rank observable and uniformly observable in the inputs. Therefore, an adequate coordinate transformation can be obtained by following the methodology presented in [32].

Consider system (15) and define the map

$$\mathbf{T}(\mathbf{x}, \mathbf{I}) = \begin{bmatrix} \mathbf{T}_{fc} \\ \mathbf{K}_1(\mathbf{E}_{thn_{cell}} - \mathbf{V}_{fc})\mathbf{I} \end{bmatrix} \triangleq \boldsymbol{\xi}, \quad (22)$$

which, as the Jacobian of (22) is full rank in the fuel cell operating region (21), is a diffeomorphism.

The map (22) is an invertible coordinate change that transforms system (15) to the following triangular form [32]

$$\dot{\boldsymbol{\xi}} = \mathbf{A}\boldsymbol{\xi} + \Psi(\boldsymbol{\xi}, \mathbf{u}), \quad (23)$$

$$y = \mathbf{c}\boldsymbol{\xi} \quad (24)$$

where

$$\mathbf{A} = \begin{bmatrix} 0 & 1 \\ 0 & 0 \end{bmatrix}; \quad \mathbf{c} = \begin{bmatrix} 1 \\ 0 \end{bmatrix}^\top \quad (25)$$

$$\Psi(\boldsymbol{\xi}, \mathbf{u}) = \begin{bmatrix} \psi_1(\xi_1, \mathbf{u}) \\ \psi_2(\boldsymbol{\xi}, \mathbf{u}, \dot{\mathbf{I}}) \end{bmatrix} \quad (26)$$

and the functions ψ_1 and ψ_2 are Lipschitz.

The triangular structure (23) is not the phase variable form studied in the past sections. However, as it will be shown in the next section, the low-power observer can be implemented in this form with minor changes in the observer structure.

Remark 4.2. *Notice that the function ψ_2 depends on the derivative of the current, $\dot{\mathbf{I}}$, which is not directly measured. Nevertheless, there are multiple ways to deal with this problem. In some types of control, one has access to the derivatives of the input, e.g. backstepping control or higher-order sliding mode control, between others. Therefore, the derivative of the input is not measured, but known. Alternatively, one can estimate its value through robust differentiators [48] and deal with the discrepancy by increasing the high-gain design parameter.*

4.3. Observer Equations

The states of the fuel cell model (15) are going to be estimated through the proposed low-power peaking-free observer with dynamic dead-zone filtering

(12), which can be directed implemented in the triangular form (23) as follows

$$\begin{aligned}
\dot{\hat{\xi}}_1 &= \eta_1 + \psi_1(\hat{\xi}_1, \mathbf{u}) + \frac{\alpha_1}{\varepsilon} \mathrm{d}z_{\sqrt{\sigma_1}}(\mathbf{e}_1) \\
\dot{\hat{\xi}}_2 &= \psi_2(\hat{\boldsymbol{\xi}}, \mathbf{u}, 0) + \frac{\alpha_2}{\varepsilon} \mathrm{d}z_{\sqrt{\sigma_2}}(\mathbf{e}_2) \\
\dot{\eta}_1 &= \psi_2(\hat{\boldsymbol{\xi}}, \mathbf{u}, 0) + \frac{\beta_1}{\varepsilon^2} \mathrm{d}z_{\sqrt{\sigma_1}}(\mathbf{e}_1) \\
\dot{\sigma}_i &= -\frac{q_i}{\varepsilon^2} \sigma_i + p_i \varepsilon \|\mathbf{e}_i\|, \quad i = 1, 2
\end{aligned} \tag{27}$$

with

$$\begin{aligned}
\mathbf{e}_1 &\triangleq \mathbf{y} - \hat{\xi}_1, \\
\mathbf{e}_2 &\triangleq \mathrm{sat}_{r_2}(\eta_1) - \hat{\xi}_2.
\end{aligned}$$

In this work, it is assumed that there is no information about the derivative of the current, $\dot{\mathbf{I}}$. Thus, the nonlinear function ψ_2 is implemented with $\dot{\mathbf{I}} = 0$. This approximation will introduce some bias in the estimation. However, the bias can be reduced by decreasing the parameter ε .

Finally, in order to recover the states in the original coordinates, it is necessary to invert the transformation (22), i.e. find a function $\mathbf{T}^{-1}(\boldsymbol{\xi}, \mathbf{I})$ such that

$$\mathbf{x} = \mathbf{T}^{-1}(\boldsymbol{\xi}, \mathbf{I}) \tag{28}$$

which is always possible as the system is observable and the map (22) is a diffeomorphism.

The proposed observer tuning process and the main observer loop have been summarized in a flowchart, see Figure 3.

5. Numerical simulations

The proposed observer scheme has been validated through a numerical simulation in Simulink 9.1 of Matlab 2018a in a computer with an i7-8700K processor and 16 GB of RAM. In the simulation, the model (15) is going to be excited with changes in the current signal, I (Figure 4), which will induce a stack temperature profile, T_{fc} , that will be used by the proposed observer scheme in order to estimate the liquid water saturation, s .

From the observer point of view, it is assumed that there is no prior information of the unknown states. Therefore, the state estimation is initialized at an arbitrary feasible operating condition $\hat{T}_{fc} = 300$ and $\hat{s} = 0.01$.

In order to stabilize the temperature of the system, the air velocity will be controlled by a proportional integral anti-windup structure (PI+AW) [45]. The proposed observer is not used in this control scheme, consequently, this section does not focus in its design. Moreover, the generated temperature profile is corrupted with random high-frequency noise with realistic variance values, see Figure 6. Notice that the temperature dynamics are mostly hidden by the sensor's noise, which is very common in electrochemical systems. In Figure 5, it is depicted the general scheme of the simulation.

To show the benefits of the proposed observer structure. The estimation of the low-power peaking-free dead-zone observer will be compared with the

estimation of a classic high-gain observer with similar convergence rate. The parameter of the classic high-gain observer are $\alpha_1 = 0.102$, $\alpha_2 = 0.0002$ and $\varepsilon = 0.055$. The low-power peaking-free dead-zone observer design parameters are summarized in the Table 2. In Figure 7 it is depicted the evolution of the model's true liquid water saturation, the classic HGO's estimation and the low-power peaking-free dead-zone observer's estimation.

In both observers, the estimation error converges to a relative error² below 5%, within the first 150 seconds, which is an acceptable convergence rate as, in general, the water dynamics of PEMFCs requires around 1000 seconds to reach a steady-state [5]. The convergence rate of both observers is nearly identical. During the steady-state, the observer estimation oscillates as a consequence of the high-frequency noise in the temperature signal. Nonetheless, the persistent estimation error induced by the noise is significantly reduced in the low-power peaking-free dead-zone observer. In order to quantify this improvement, the mean square error (MSE) of the liquid water saturation estimation has been computed,

$$MSE = \frac{1}{n} \sum_1^n (s(i) - \hat{s}(i))^2,$$

with a sampling time of 0.1 s.

The implementation of the low-power peaking-free dead-zone observer

²The relative error [%] between x and \hat{x} is computed as $\frac{\|x - \hat{x}\|}{x} \cdot 100$

has resulted in a reduction of 32.3% of the MSE. Similar reduction of the MSE could have been achieved by increasing the value of ε or by filtering the temperature signal through a low-pass filter. However, in the former case, the robustness and convergence rate of the observer would be significantly reduced. In the latter, the convergence rate would be significantly affected.

The presented simulation serves as an example of the amount of noise reduction that can be expected from the proposed scheme. Furthermore, additional simulations have been conducted to assess the validity of the MSE error reduction in different case scenarios. In particular, the MSE reduction has been analysed for a set of different initial conditions for the fuel cell model and for a set of different sensor noise value.

For the case of different initial conditions on the fuel cell plant, the results are depicted in Figure 8 a). It can be observed that, in all cases, the proposed observer outperforms the classic HGO with at least a 36% MSE reduction. Moreover, a clear tendency can be seen that shows a further MSE reduction for large values of the temperature and low values of the liquid water saturation. This tendency can be explained by the fact that fuel cell initial conditions with large temperature values and low liquid water saturation will naturally converge to low liquid water saturation values. In such cases, the effect of the liquid water on the temperature dynamics is reduced, which, as a consequence, increases the noise sensitivity of the observer. Consequently, the significance of having filtering elements as the dynamic dead-zone filter drastically increases, which explains the result.

For the case of different values of noise power, the results are depicted in Figure 8 b). It should be remarked that the data is for the observer in steady-state. It can be seen that the MSE reduction of the proposed observer increases with the noise power. This result validates the usefulness of the technique in scenarios with very noisy sensors.

Moreover, some of these simulations validates the benefits of having a peaking-free property. An example is depicted in Figure 9. It can be seen that the classic high-gain observer drastically peaks during the transient, while the proposed observer does not present any peaking and presents a simpler transient behaviour.

In summary, this numerical simulation shows that the proposed observer reduces the noise sensibility of the classic HGO without influencing the performance in terms of convergence rate and robustness. Moreover, the proposed observer also presents the benefit of eliminating the peaking phenomena.

6. Experimental Validation

Last section validated the proposed observer in a numerical simulation where the observer is capable of accurately estimating the models states in a noisy environment. However, one cannot expect the “simulated” model to depict all the details and dynamics of the true real system. As a consequence, some conflicts may arise during the real implementation of the observer. For this reason, it is crucial to validate the proposed strategy in a

real experimental set-up, which will be the focus of this section.

6.1. Experimental Set-up

The considered PEM fuel cell system is the model H-100 of *Horizon fuel cell technologies*. This model presents a rated power of 100 W, 20 stacked cells, an open-cathode architecture with an active surface of 22.5 cm^2 and an efficiency of 40% at 12 V. The fuel cell's cathode incorporates a fan that delivers the reactant and cools the system. In order to measure the air velocity, a hot film sensor model EE75 of E+E Elektronik has been included in the cathode.

The PEMFC is operated in dead-end mode [46], with a back-pressure regulator that maintains the anode inlet pressure at 0.4 bar. This architecture allows avoiding the need of a flow controller. Nonetheless, it is required to periodically purge the system. Specifically, 500 ms purges in the anode are executed at a period of 20 seconds.

The PEM fuel cell obtains the reactant from the ambient air. Consequently, the operation of the system is very sensitive to the ambient conditions. In order to make the experiments repeatable, the fuel cell is enclosed in an environmental chamber that regulates the ambient temperature, relative humidity and oxygen concentration.

The environmental chamber includes its own sensors, for ambient conditions control purposes. Nevertheless, the humidity and temperature of the ambient are measured through a sensor HMM211 from Vaisala. Moreover,

the temperature of each cell is measured, through a type K thermocouple pt1000. The average of all the thermocouple measurements is considered as the stack temperature (T_{fc}).

The experimental set-up includes a programmable load that allows to control the exchange current. The voltage of each individual cell is measured through an isolation amplifier, HCPL-788J from Agilent Technologies and the exchange current (I) through a Hall effect sensor model LTS 6 NP of LEM. The sensors of the experimental prototype and its specifications are summarized in Table 3.

The sensors are connected to a controller cRIO-9047 of National Instruments, which is programmed in the LabView environment. The test station presents a processor of 16 *GHz*, 4 *GB* of DRAM and a SSD of 4 *GB*. The sampling time of the data acquisition is of 2 *s*, which is considered to be adequate, as the time scales of thermal and water dynamics time are an order of magnitude larger.

In Figure 10 it is depicted a scheme of the experimental set-up and in Figure 11 it is depicted the environmental chamber and the H-100 PEM fuel cell.

6.2. Methodology

The H-100 PEM fuel cell setup will be excited by a constant current of 3.8 *A*, and the cathode air velocity profile depicted in Figure 12.

Exciting the system with these profiles places the observer in an interest-

ing position. On the one hand, due to the cathode air velocity's decrease, the fuel cell's stack temperature is expected to increase, which will boost the liquid water evaporation rates and overcome the generation of water due to the reduction reaction. Consequently, the liquid water saturation, s , should reduce during the experiment. On the other hand, the abrupt change in the cathode air velocity will induce a fast change in the stack temperature, T_{fc} , which, as a direct consequence, will significantly increase the state estimation error during a certain time. If the observer presents the peaking phenomena, this increase in the estimation error will be significantly aggravated and can make the estimation practically unusable. The experiment conditions are summarized in Table 4.

The proposed input profiles induced the temperature and voltage profiles presented in Figure 13 and Figure 14, respectively. Notice that the measured voltage profile present some periodic downward peaks, which are the consequence of the periodic purges of the anode due to the dead-end mode operation [46].

The temperature profile, Figure 13, is introduced in the observer in order to estimate on-line the liquid water saturation. The main concern in validating the proposed observer strategy is the unavailability of sensors that can directly measure the variable, s . Consequently, the estimation generated by the proposed technique, \hat{s} , cannot be contrasted with the true values, as they are not being measured. However, there are other measured signals that can be used to validate the estimation.

The estimation of the stack temperature, \hat{T}_{fc} , the estimation of the liquid water, \hat{s} , and the voltage equation (14) can be used to generate an estimation of the stack voltage, \hat{V}_{fc} . If we assume that the model is accurate, the stack voltage only depends on the stack temperature and the CCL's liquid water saturation. As the stack voltage and temperature are actually measured, one can verify the accuracy of the liquid water estimation by computing the estimation errors $\|T_{fc} - \hat{T}_{fc}\|$ and $\|V_{fc} - \hat{V}_{fc}\|$, i.e., if the stack temperature and the voltage estimation are accurate, we can assume that the liquid water estimation is also accurate.

6.3. Results

The experimental profiles of current (Figure 4), air velocity (Figure 12) and stack temperature (Figure 13) has been introduced in the proposed observer and, as a consequence, an estimation of the liquid water saturation has been generated, Figure 15.

Notice that the estimation converges to a value around 0.1 kg m^{-2} , in 200 seconds, which is coherent with the values obtained in the simulation, Figure 7. Moreover, it can be seen that the liquid water saturation is slowly decreasing. This tendency was predicted during the experiment design, as an increase of the temperature results in a boost of the water evaporation rates.

Notice that around second 400 and around second 2000 there are some peaks. These peaks are the consequence of the abrupt change in the cath-

ode's air velocity, Figure 12, which induces a sudden change in the stack temperature, Figure 13, and an increase of the estimation error, which affects the estimation of the liquid water saturation. In the classic HGO, these abrupt changes would be amplified due to the peaking phenomena, making the estimation practically unusable. Indeed, a HGO with a settling time of 200 seconds presents a peak at time 2000 seconds that exceeds s_{opt} (see Table 5). Therefore, the states of a classic HGO leave the domain (21) and the system becomes unobservable, which will make the transformation (22) not injective and the estimation of the observer unusable. Thus, the presence of the peaking phenomena makes the presented estimation problem not solvable through a HGO. However, the presented peaking-free modification stabilizes the estimation in less than 300 seconds and the estimation, \hat{s} , does not surpass the value s_{opt} . Therefore, the system is always observable.

Moreover, the measurement noise present in the temperature profile induces some noisy oscillations in the liquid water estimation. Nevertheless, the amplitude of the oscillations is below 1% and can be neglected. Notice, that if a classic HGO was applied, this error would be an order of magnitude larger, and the estimation would be practically unusable.

In order to validate the accuracy of the estimation, the measured stack temperature profile and output voltage profile will be used. Specifically, in Figure 16, it is depicted the measured temperature profile and the observer's estimation. It can be seen that, after the transient, the relative error is below the 0.1%.

In Figure 17 it is depicted the output voltage profile and the observer's estimation (computed through (14)). The estimation can be defined as accurate, as the relative error converges to a value below the 0.5%. The abrupt changes around second 400 and second 2000 are due to the changes in the cathode air velocity, Figure 12. However, it can be seen that after the abrupt changes, the estimation stabilizes again around the relative error 0.5%.

As the temperature and voltage estimation converges to a relative error below the 0.5%, it can be concluded that the CCL's liquid water saturation estimation is accurate. Nevertheless, the voltage estimation slightly undershoots the true value. This discrepancy it is due to the uncertainty in the voltage equation. Indeed, the voltage estimation, \hat{V}_{fc} , is achieved outside the observer's loop; therefore, the uncertainty's effect is not reduced by the observer's feedback nature. Notice that this does not happen in the temperature estimation, Figure 16. As the temperature estimation is achieved inside the observer's loop, even in the presence of model discrepancies, the estimation converges to a low relative error. The liquid water saturation estimation, \hat{s} , is also achieved inside the observer's loop, so, it is expected to be robust to the model uncertainties and more accurate than the voltage estimation.

6.4. Feasibility of the proposed observer

The experimental implementation of the proposed scheme has shown positive results, which validates the possibility of implementing the observer in

a real PEMFC. The base of the proposed scheme is the substitution of the common high-gain observer with a novel low-power peaking-free dead-zone observer. The main benefits of this substitution are a significant reduction of the observer noise sensitivity, a diminution of 32.3% in the MSE, and the elimination of the peaking phenomena without deteriorating the transient of the observer and without an increase of the number of assumptions through the observer tuning. Moreover, the proposed approach requires the same sensors of the common HGO.

Nonetheless, the improvement comes with the cost of increasing the order of the observer, from order 2 of the standard high-gain observer to order 5, which increases the computation cost of the observer. It is crucial to study if this increase compromises the technological and economical feasibility of the proposed solution.

A method to carry on with this analysis is to compare the computational cost of a single iteration of the high-gain observer with a single iteration of the low-power peaking-free dead-zone observer. For this purpose, it is convenient to discretize in time the equations of the observer. Specifically, assume that there is an observer, the dynamics of which are depicted as:

$$\dot{\hat{\mathbf{x}}} = \mathbf{g}(\hat{\mathbf{x}}, \mathbf{u}, y)$$

where \mathbf{g} is a vector of (nonlinear) functions.

Then, one can approximately discretize the observer at a sampling time

τ_s through the Euler method as:

$$\hat{\mathbf{x}}(k+1) = \hat{\mathbf{x}}(k) + \tau_s \mathbf{g}(\hat{\mathbf{x}}(k), \mathbf{u}(k), y(k)).$$

Consequently, to compare the computational cost of one observer to another, it is sufficient to compare the computational time of the function $\mathbf{g}(\hat{\mathbf{x}}(k), \mathbf{u}(k), y(k))$.

This analysis has been carried on in Matlab 2018a in a computer with an i7-8700K processor and 16 GB of RAM, where it has been compared the computation cost of the high-gain observer and the low-power peaking-free observer along a realistic trajectory of the system. On the one hand, the cost of one iteration of the high-gain observer has resulted in an average time of $4.455 \cdot 10^{-6}$ s (variance $5.680 \cdot 10^{-12}$ s²). On the other, the low-power peaking-free dead-zone observer has resulted in an average time of $5.184 \cdot 10^{-6}$ s (variance $1.0822 \cdot 10^{-12}$ s²), which is an increment of 16.36%. Notice that the sampling time considered in the experimental prototype is of 2 s. Consequently, in both cases, the computational cost of the observer is below the $3 \cdot 10^{-4}\%$, which makes the increment in the computational cost negligible.

7. Conclusions

This work has presented a nonlinear observer for the estimation of the liquid water saturation in PEMFC systems. The observer combines the ideas

of the low-power peaking-free observer and dynamic dead-zone filtering in order to create a new observer that out-performs the classic HGO. This new observer could serve as a way of implementing HGO-based control algorithms in the PEMFC active water management problem. The viability of the observer has been shown through a rigorous proof, numerical simulations and experimental validation. In the validations, it is shown a reduction of the mean square error of 32.3% with respect to a classical high-gain observer with similar convergence rate and robustness. Moreover, the elimination of the peaking phenomena prevents the state estimation to drift outside the operating region, which allows to maintain the observability of the system and allows to implement the observer in a real experimental prototype.

Future works will focus on combining the proposed observer with an on-line identification algorithms in order to estimate simultaneously the liquid water saturation and unknown parameters related to the water dynamics.

Acknowledgements

This work has been partially funded by the Spanish Ministry of Universities funded by the European Union - NextGenerationEU (2022UPC-MSC-93823). This work is part of the Project MAFALDA (PID2021-126001OB-C31) funded by MCIN/ AEI /10.13039/501100011033 and by "ERDF A way of making Europe". This work is part of the project MASHED (TED2021-129927B-I00), funded by MCIN/ AEI/10.13039/501100011033 and by the European Union Next GenerationEU/PRTR.

Tables

Table 1: Nomenclature and abbreviations

Symbol	Definition
PEMFC variables	
T_{fc}	Stack temperature
s	Cathode catalyst layer liquid water saturation
V_{fc}	Stack voltage
I	Exchange current
v_{air}	Cathode air velocity
RH_{amb}	Ambient relative humidity
T_{amb}	Ambient temperature
PEMFC parameters	
n_{cell}	Number of cells
m_{fc}	Stack mass
$C_{p,fc}$	PEMFC specific heat
A_{inlet}	Inlet cross-sectional area
Θ	Effective control angle
K_s	Liquid water accumulation coefficient
A_{geo}	Cathode catalyst layer surface area
K_{evap}	Evaporation time constant
A_{pore}	Pore surface per unit volume
ϵ_{eff}	Cathode catalyst layer effective porosity

K_{eff}	Cathode catalyst layer effective permeability
α	Transfer coefficient
d_{diff}	Cathode catalyst layer width
E_{th}	Theoretical potential of a cell
R_{ohm}	PEMFC ohmic resistance
j_0^{ref}	Reference exchange current
a_c	Electrode rugosity
T_{ref}	Reference temperature
Physical constants	
ρ_{air}	Air density
$C_{p,air}$	Air heat capacity
p^0	Pre-exponential evaporation factor
K_b	Boltzmann's constant
E_a	Activation energy of the evaporation process
F	Faraday's constant
ΔG^*	Activation energy of the reduction reaction
M_{H_2O}	Water molar mass
R	Ideal gas constant
σ_w	Water surface tension
ρ_l	Water density
μ_l	Water viscosity
s_{opt}	Optimal liquid water saturation

Observer states	
$\hat{\xi}$	Observer internal states
η	Observer redundant state
σ	Dynamic dead-zone amplitudes
\hat{x}	State estimation
e	State estimation error
Observer parameters	
α, β	Observer gain coefficients
ε	Observer high-gain parameter
r_i	Saturation function constant
q_i	Dynamic dead-zone time constant
p_i	Dynamic dead-zone steady-state gain
Abbreviations	
PEMFC	Polymer electrolyte membrane fuel cell
CCL	Cathode catalyst layer
HGO	High-gain observer
LPPFDZO	Low-power peaking-free dead-zone observer
PI	Proportional integral
AW	Anti wind-up
MSE	Mean square error

Table 2: Low-power peaking-free dead-zone observer parameters

Parameter	Value
α_1	1.5
α_2	0.01
β_1	0.5
r_1	0.16
ε	0.25
q_i	3
p_1	180
p_2	40

Table 3: Sensors of the experimental prototype

Variable	Sensor	Range	Bandwidth/Response time (τ_s)	Accuracy
v_{air}	EE75	0 – 2 m/s	$\tau_s = 1.5 s$	$\pm 0.03 m/s$
RH_{ca}	HMM211	0 – 100% RH	$\tau_s = 15 s$	$\pm 2\% RH$
T_{fc}	<i>pt1000</i>	–50 – 203°C	-	$\pm 0.5^\circ C$
V_{fc}	HCPL-788J	0 – 6 V	30 Khz	$\pm 0.6\%$
I	LTS6NP	0 – 19.2 A	100 Khz	$\pm 0.2\%$
T_{amb}	HMM211	–70 – 180°C	-	$\pm 0.1^\circ C$

Table 4: Experiment conditions

Factor	Value	Units
Anode reactant	H_2	–
Cathode reactant	Ambient air (21% O_2)	–
T_{amb}	25	$^\circ C$
RH_{amb}	75	%
Anode Pressure	0.4	<i>Bar</i>
Anode RH	0	%
Current	3.98	A

Table 5: Parameters of the fuel cell model

Parameter	Value	Units
m_{fc}	0.324	kg
$C_{p,fc}$	1297	$Jkg^{-1}K^{-1}$
E_{th}	1.085	V
ρ_{air}	1.07	$kg\ m^{-3}$
A_{inlet}	$8.7E - 3$	m^2
$C_{p,air}$	1005	$Jkg^{-1}K^{-1}$
T_{amb}	298	K
A_{geo}	0.00225	m^2
K_s	0.149	$kg\ m^{-2}$
K_{evap}	$8.4E5$	$kg\ s^{-1}\ m^{-2}$
A_{pore}	$2.2E7$	m^2m^{-3}
p^0	$1.196E11$	Pa
E_a	0.449	eV
p_v	2380	Pa
σ_w	0.0673	$N\ m^{-1}$
Θ	1.5882	rad
ϵ_{eff}	0.536	–
K_{eff}	$9.97E - 15$	m^2
ρ_l	997	kg/m^3
μ_l	$3.587E - 4$	$Pa\ s$
d_{diff}	$4.1E - 4$	m
n_{cell}	20	–
α	0.311	–
a_c	238	–
j_0^{ref}	$4.7E - 3$	$A\ m^{-2}$
ΔG^*	70000	J/mol
R_{ohm}	0.33	Ω
s_{opt}	0.165	$kg\ m^{-2}$

Figures

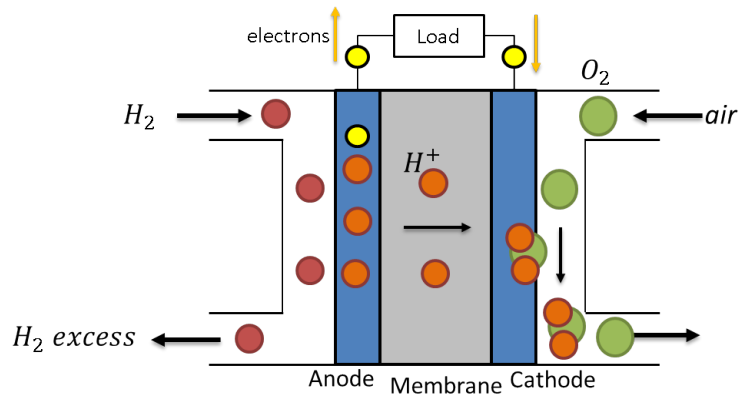


Figure 1: General scheme of a single PEM fuel cell operation.

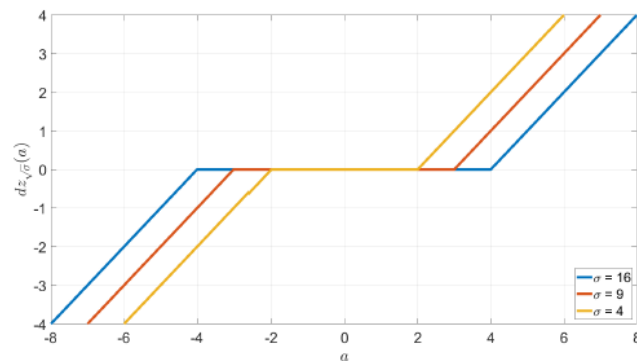


Figure 2: Dead-zone function with $\sigma = 4$, $\sigma = 9$ and $\sigma = 16$.

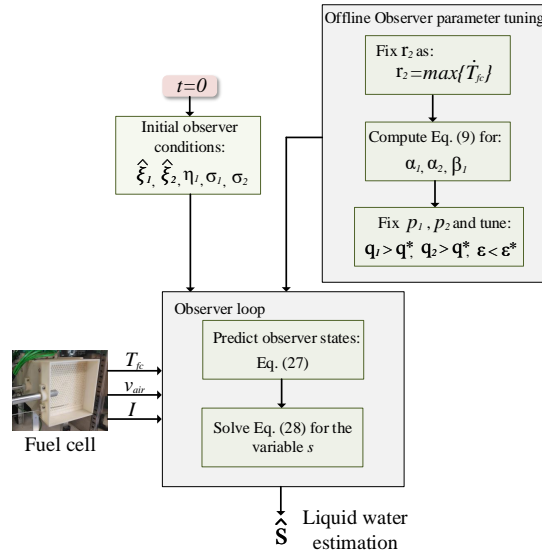


Figure 3: General flowchart of observer offline tuning and online implementation.

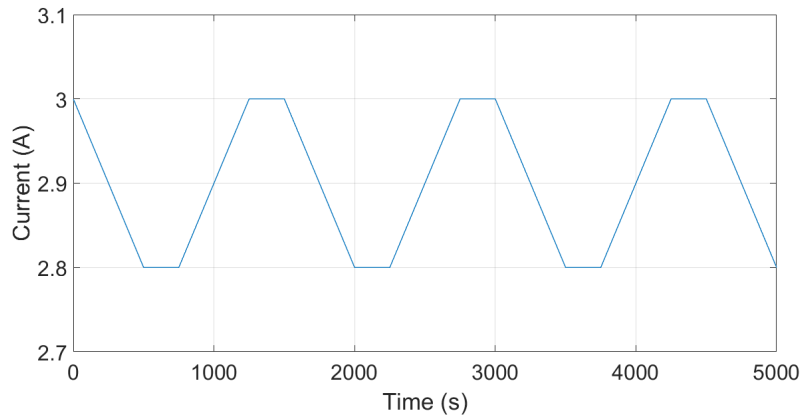


Figure 4: Current profile used to excite the simulated model.

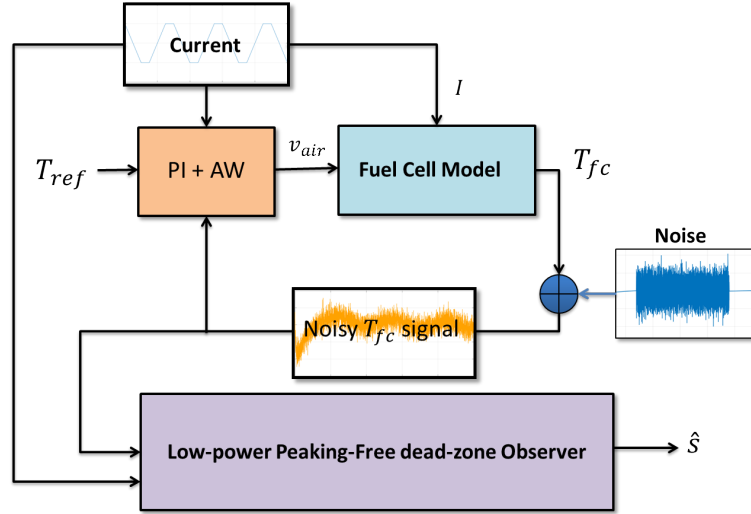


Figure 5: General scheme of the simulation. The PI+AW box depicts the controller proposed in [45], the fuel cell model box depicts the model (15) with the parameters summarized in Table 5 and the low-power power-peaking-free dead-zone observer box depicts the proposed observer scheme.

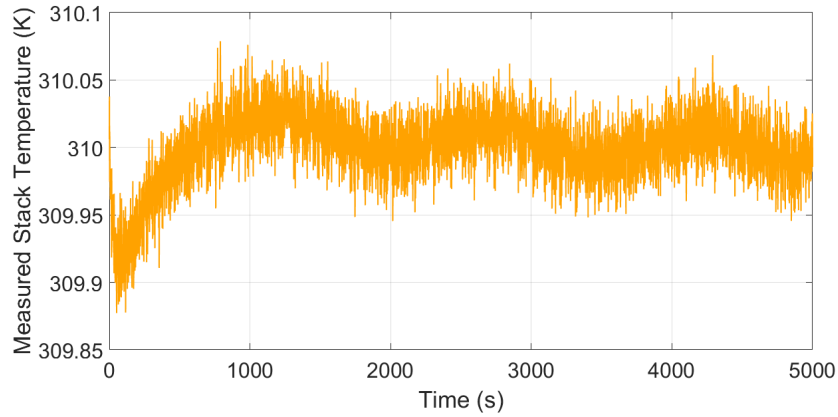


Figure 6: Model's measured temperature signal corrupted with Gaussian noise.

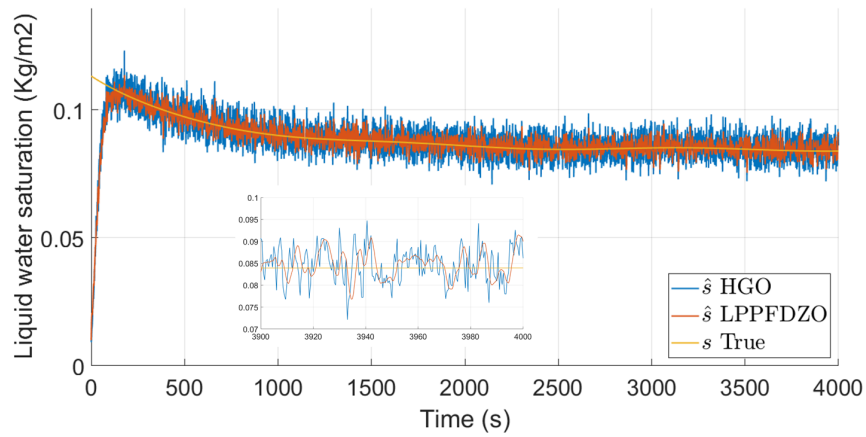


Figure 7: Model's liquid water saturation (yellow), HGO estimation (blue) and low-power peaking-free dead-zone observer (LPPFDZO) estimation (orange) in presence of measurement noise.

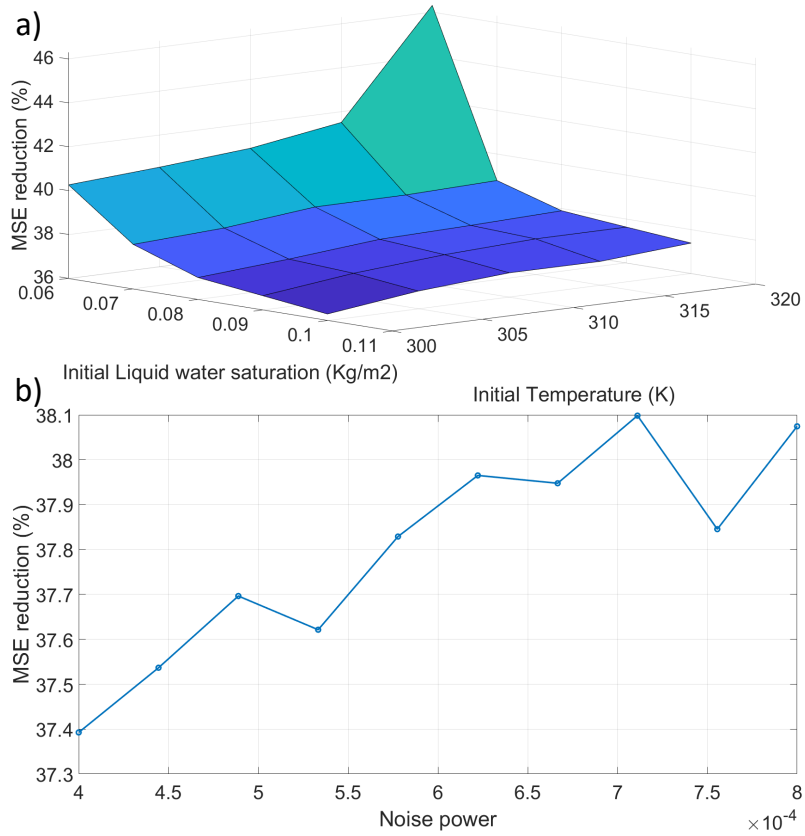


Figure 8: a) MSE reduction of the proposed observer over the classic high-gain observer with different initial conditions in the fuel cell model. b) MSE reduction of the proposed observer with different values of noise power. The fuel cell model initial conditions on the case b) have been fixed as $T_{fc} = 320$ and $s = 0.1$.

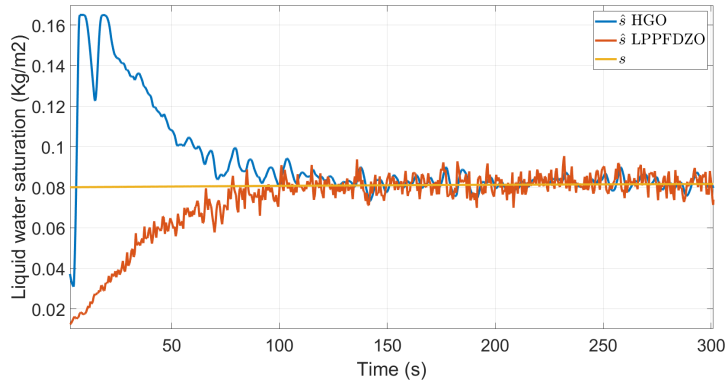


Figure 9: Classic HGO CCL's liquid water saturation estimation, low-power peaking-free dead-zone observer estimation and true value of the liquid water saturation

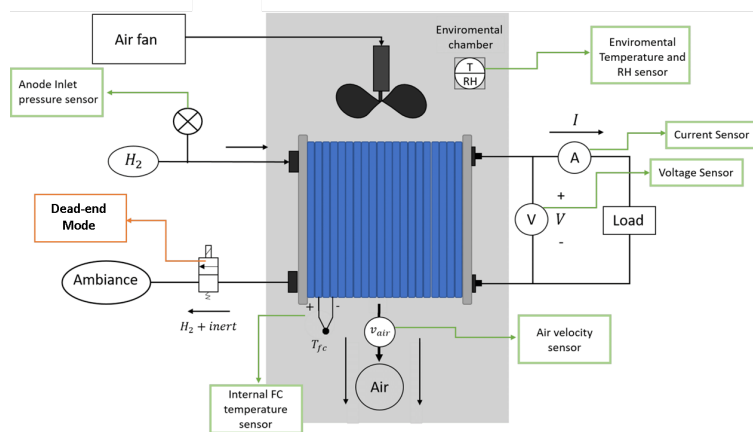


Figure 10: H-100 experimental set-up scheme.

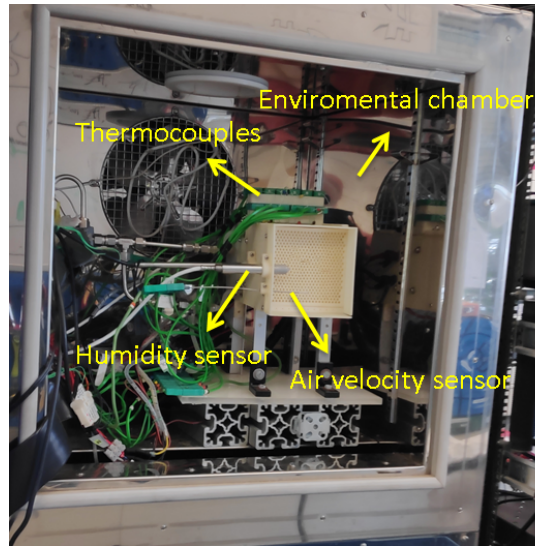


Figure 11: Environmental chamber and H-100 PEM fuel cell.

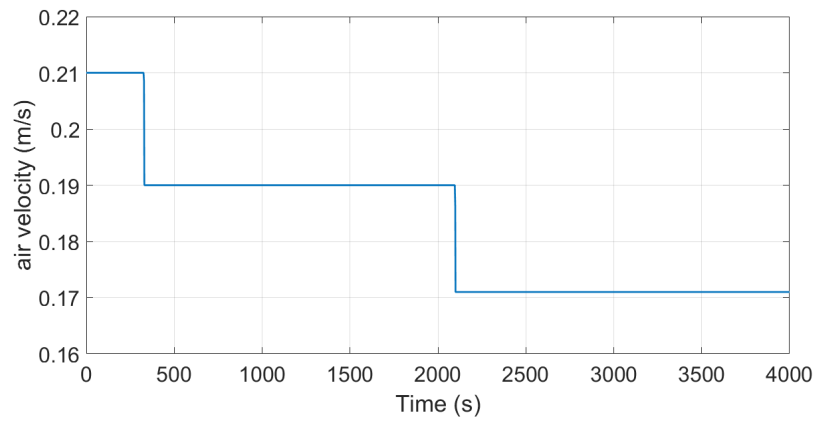


Figure 12: Implemented cathode's air velocity.

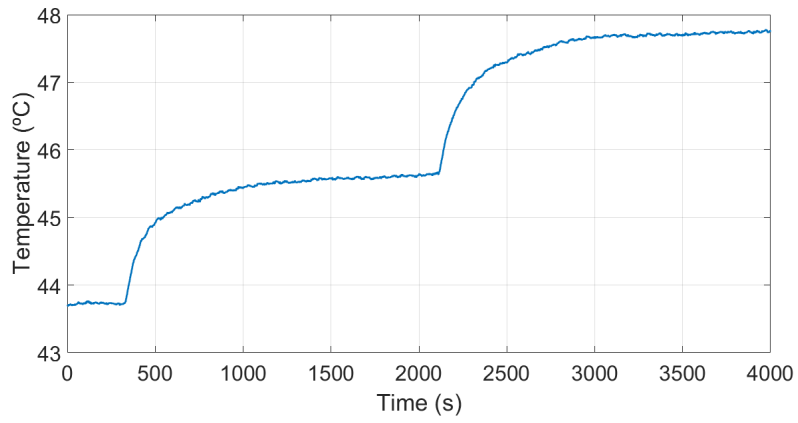


Figure 13: Measured stack temperature profile.

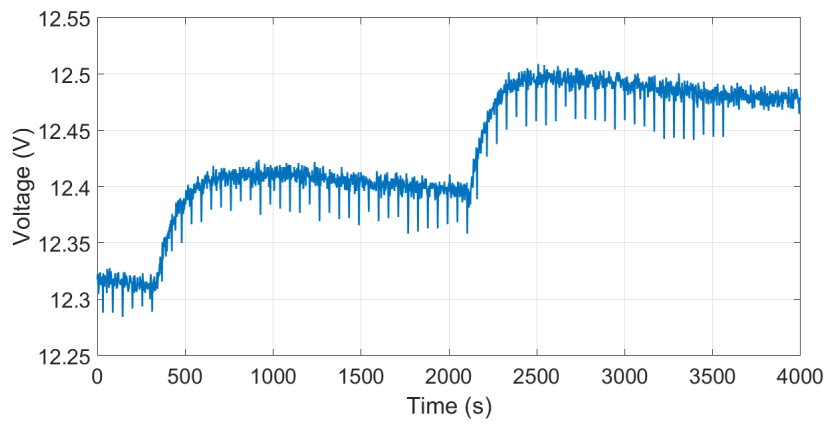


Figure 14: Measured voltage profile.

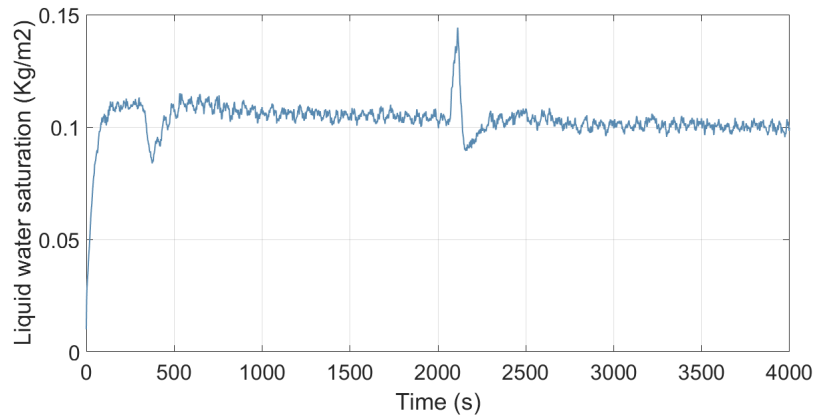


Figure 15: Low-power peaking-free dead-zone observer CCL's liquid water saturation estimation.

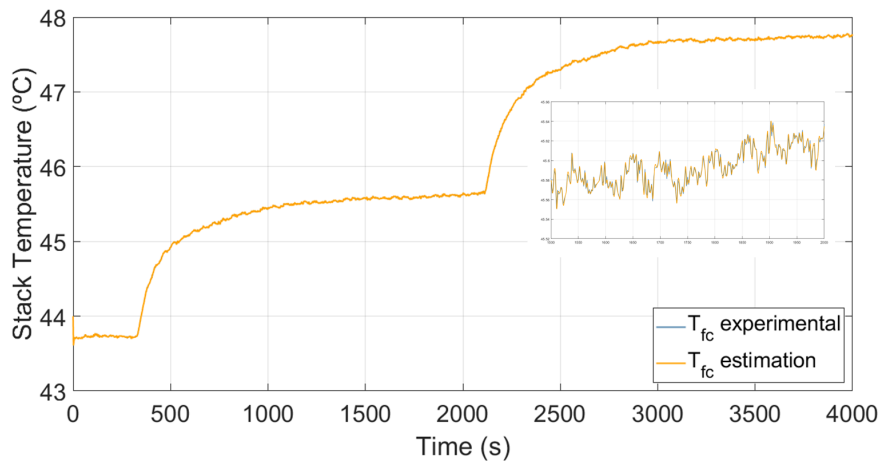


Figure 16: Measured stack temperature profile (blue) and adaptive observer's estimation (yellow).

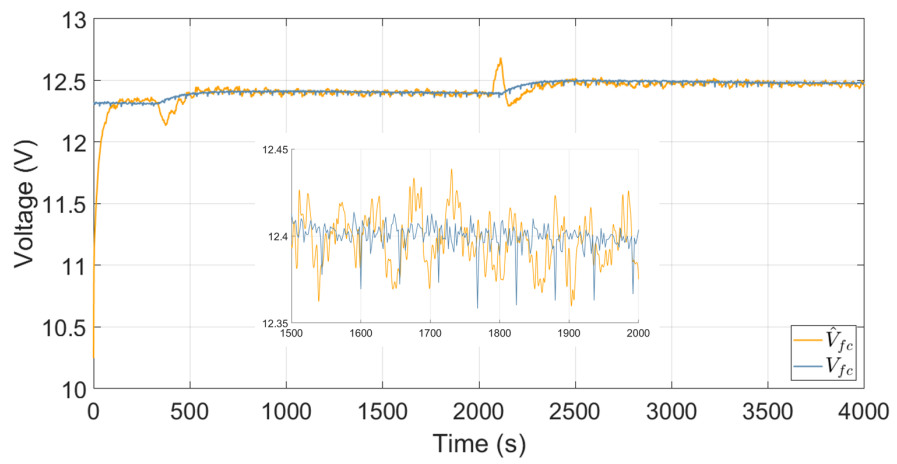


Figure 17: Measured output voltage profile (blue) and adaptive observer's estimation (yellow).

Appendix A. Theorem 2.1 proof

This proof is a sketched version of the one presented in [22].

Define the following scaled errors

$$\eta_1 = \frac{x_1 - \hat{x}_1}{\varepsilon^{n-1}}, \quad \eta_2 = \frac{x_2 - \hat{x}_2}{\varepsilon^{n-2}}, \dots, \quad \eta_n = x_n - \hat{x}_n. \quad (\text{A.1})$$

The dynamics of $\boldsymbol{\eta} \triangleq [\eta_1, \dots, \eta_n]^\top$ are depicted by the following expression

$$\varepsilon \dot{\boldsymbol{\eta}} = \mathbf{A}_{cl} \boldsymbol{\eta} + \varepsilon \boldsymbol{\delta}(\mathbf{x}, \hat{\mathbf{x}}, \mathbf{d}) - \frac{1}{\varepsilon^{n-1}} \mathbf{E}v$$

where

$$\boldsymbol{\delta} = \text{col}(0, \dots, 0, \delta_n), \quad \mathbf{E} = [\alpha_1, \dots, \alpha_n]^\top$$

and δ_n is

$$\delta_n = \boldsymbol{\phi}(\mathbf{x}, \mathbf{d}) - \boldsymbol{\phi}(\hat{\mathbf{x}}, 0).$$

By means of the Lipschitz condition (2), it is possible to show that for all $\varepsilon \leq 1$

$$\|\boldsymbol{\delta}\| \leq L_\phi \|\boldsymbol{\eta}\| + \|\boldsymbol{\phi}(\mathbf{x}, \mathbf{d}) - \boldsymbol{\phi}(\mathbf{x}, 0)\| \triangleq L_\phi \|\boldsymbol{\eta}\| + M. \quad (\text{A.2})$$

Consider the positive definite and radially unbounded Lyapunov function

$$V = \boldsymbol{\eta}^\top \mathbf{P} \boldsymbol{\eta}. \quad (\text{A.3})$$

The derivative of (A.3) satisfies the following

$$\begin{aligned}\varepsilon\dot{V} &= -\boldsymbol{\eta}^\top \boldsymbol{\eta} + 2\varepsilon\boldsymbol{\eta}^\top \mathbf{P}\delta - \frac{2}{\varepsilon^{n-1}}\boldsymbol{\eta}^\top \mathbf{P}\mathbf{E}v \leq -\|\boldsymbol{\eta}\|^2 + 2\varepsilon L_\phi \|\mathbf{P}\| \|\boldsymbol{\eta}\|^2 \\ &\quad + 2\varepsilon \|\mathbf{P}\| \|\boldsymbol{\eta}\| M + \frac{2}{\varepsilon^{n-1}} \|\mathbf{P}\mathbf{E}\| \|\boldsymbol{\eta}\| \|v\|_\infty\end{aligned}\tag{A.4}$$

By inspection of the first two elements in the right hand side of (A.4), it can be seen that for all $\varepsilon \leq \frac{1}{2L_\phi \|\mathbf{P}\|}$ inequality (A.4) reduces to

$$\begin{aligned}\varepsilon\dot{V} &\leq -c\|\boldsymbol{\eta}\|^2 + 2\varepsilon \|\mathbf{P}\| \|\boldsymbol{\eta}\| M + \frac{2}{\varepsilon^{n-1}} \|\mathbf{P}\mathbf{E}\| \|\boldsymbol{\eta}\| \|v\|_\infty, \\ \varepsilon\dot{V} &\leq -\frac{c}{2}\|\boldsymbol{\eta}\|^2 \quad \forall \|\boldsymbol{\eta}\| \geq 4\left(\varepsilon \|\mathbf{P}\| \|\boldsymbol{\eta}\| M + \frac{1}{\varepsilon^{n-1}} \|\mathbf{P}\mathbf{E}\| \|\boldsymbol{\eta}\| \|v\|_\infty\right)\end{aligned}$$

where c is a positive constant dependent of ε .

As a consequence, by applying Theorem 4.5 of [49] and inverting the coordinate change (A.1), the bound (6) can be proved.

Appendix B. Theorem 2.2 proof

This proof is a sketched version of the proof presented by Astolfi *et. al* in [28].

First, define the following change of coordinates

$$\begin{aligned}\xi_i &\triangleq [x_i - \hat{x}_i, \varepsilon(x_{i+1} - \eta_i)]^\top, \quad i = 1, \dots, n-1 \\ \xi_n &\triangleq x_n - \hat{x}_n\end{aligned}\tag{B.1}$$

The dynamics of the transformed systems are governed by

$$\begin{aligned}\dot{\xi}_i &= \frac{1}{\varepsilon} \mathbf{E}_i \xi_i + \varepsilon \mathbf{B}_2 \bar{u}_i + \frac{1}{\varepsilon} \begin{bmatrix} \alpha_i \\ \beta_i \end{bmatrix} \bar{w}_i \\ \dot{\xi}_n &= -\frac{\alpha_n}{\varepsilon} \xi_n + \bar{u}_{n-1} + \frac{1}{\varepsilon} \bar{w}_n\end{aligned}$$

where $\bar{w}_1 = v$ and $\bar{w}_i = -\text{sat}_{r_i}(\eta_{i-1})$ for $i = 2, \dots, n$, $\bar{u}_i = \mathbf{x}_{i+2} - \text{sat}_{r_{i+2}}(\eta_{i+1})$ for $i = 1, \dots, n-2$ and $\bar{u}_{n-1} = \phi(\hat{\mathbf{x}}, 0) - \phi(\mathbf{x}, \mathbf{d})$.

By virtue of (9), the matrices \mathbf{E}_i are Hurwitz. Moreover, since \mathbf{x} and \mathbf{d} evolve in a compact set the variable u_i is upper-bounded by a positive constant. Finally, the factors \bar{w}_i are also upper-bounded by a positive constant. Taking into account these details, considering (9) and following some Lyapunov arguments similar to the ones in Theorem's 2.1 proof (Lemma 5 of [28]), it is possible to show that, if ε is small enough, the following holds

$$\|\xi_i\| \leq c_{1i} e^{\frac{-c_{2i}}{\varepsilon} t} \|\xi_i(0)\| + \varepsilon^2 c_{3i} u_i + c_{4i}$$

where c_{1i}, \dots, c_{4i} for $i = 1, \dots, n$ are some positive constants independent from ε .

Moreover, the following bound holds by definition of the coordinate change (B.1)

$$\|\mathbf{x}_i - \hat{\mathbf{x}}_i\| \leq \|\xi_i\| \tag{B.2}$$

Second, if the matrix inequality (9) is satisfied and $\|v\|_\infty$ is small enough,

the virtual states η_i will exit the saturation (if it is reached), which will recover the classic high-gain observer convergence (6) [28].

As a consequence, the bound (10) can be immediately deduced with $\bar{p}_i = c_{1i} \max_{\mathbf{x}, \eta} \{ \|x_i - \hat{x}_i\| + \|x_{i+1} - \eta_i\| \} + c_{3i} \|\bar{u}_i\|_\infty + c_{4i}$.

Appendix C. Theorem 2.3 proof

Define the coordinate change (B.1). The dynamics of the coordinates, ξ_i , are depicted by

$$\dot{\xi}_1 = \frac{1}{\varepsilon} \mathbf{E}_1 \xi_1 + \varepsilon \mathbf{B}_2 (x_3 - \text{sat}_{r_3}(\eta_2)) + \frac{1}{\varepsilon} \begin{bmatrix} \alpha_1 \\ \beta_1 \end{bmatrix} v + \frac{1}{\varepsilon} \begin{bmatrix} \alpha_1 \\ \beta_1 \end{bmatrix} \text{sat}_{\sqrt{\sigma_1}}(x_1 - \hat{x}_1 + v) \quad (\text{C.1})$$

for $i = 2, \dots, n-1$

$$\begin{aligned} \dot{\xi}_i &= \frac{1}{\varepsilon} \mathbf{E}_i \xi_i + \varepsilon \mathbf{B}_2 (x_{i+2} - \text{sat}_{r_{i+1}}(\eta_i)) - \frac{1}{\varepsilon} \begin{bmatrix} \alpha_i \\ \beta_i \end{bmatrix} (x_i - \text{sat}_{r_i}(\eta_{i-1})) \\ &+ \frac{1}{\varepsilon} \begin{bmatrix} \alpha_i \\ \beta_i \end{bmatrix} \text{sat}_{\sqrt{\sigma_i}}(\text{sat}_{r_i}(\eta_{i-1}) - \hat{x}_i) \end{aligned} \quad (\text{C.2})$$

$$\begin{aligned} \dot{\xi}_n &= \frac{1}{\varepsilon} \alpha_n \xi_n + \phi(\hat{\mathbf{x}}, 0) - \phi(\mathbf{x}, \mathbf{d}) - \frac{1}{\varepsilon} \alpha_n (x_n - \text{sat}_{r_n}(\eta_{n-1})) \\ &+ \frac{1}{\varepsilon} \alpha_n \text{sat}_{\sqrt{\sigma_n}}(\text{sat}_{r_n}(\eta_{n-1}) - \hat{x}_n) \end{aligned} \quad (\text{C.3})$$

Now consider the radially unbounded Lyapunov function

$$V_1 = \xi_1^\top \mathbf{P}_1 \xi_1 + \sigma_1 \quad (\text{C.4})$$

where \mathbf{P}_i is symmetric positive definite matrix such that

$$\mathbf{P}_1 \mathbf{E}_1 + \mathbf{E}_1^\top \mathbf{P}_1 = -\mathbf{I}$$

The derivative of the Lyapunov function (C.4) satisfies

$$\dot{V}_1 \leq -\frac{1}{\varepsilon} \xi_1^\top \xi_1 + 2\xi_1^\top \mathbf{P}_1 \varepsilon \mathbf{B}_2 (\mathbf{x}_3 - \text{sat}_{r_3}(\eta_2)) + \frac{2}{\varepsilon} \xi_1^\top \mathbf{P}_1 \begin{bmatrix} \alpha_1 \\ \beta_1 \end{bmatrix} (\mathbf{v} + \text{sat}_{\sqrt{\sigma_1}}(\mathbf{x}_1 - \hat{\mathbf{x}}_1 + \mathbf{v})) - \frac{q_1}{\varepsilon^2} \sigma_1 + p_1 \varepsilon \|\mathbf{e}_1\|$$

As the states $\mathbf{x} \in X$ and $\|\text{sat}_{r_3}(\eta_2)\| \leq r_3$ its easy to see that $\|\mathbf{x}_3 - \text{sat}_{r_3}(\eta_2)\| \leq c_1$, where c_1 is a positive constant. Moreover, notice that $\|\text{sat}_{\sqrt{\sigma_1}}(\mathbf{x}_1 - \hat{\mathbf{x}}_1 + \mathbf{v})\| \leq \|\sqrt{\sigma_1}\|$ and $\|\mathbf{e}_1\| \leq \|\xi_1\|$, by definition. Therefore, the time derivative of V_1 can be upper bounded as

$$\begin{aligned} \dot{V}_1 \leq & -\frac{1}{\varepsilon} \|\xi_1\|^2 + 2\|\xi_1\| \|\mathbf{P}_1\| \varepsilon \|\mathbf{B}_2\| c_1 + 4\|\xi_1\|^2 \|\mathbf{P}_1\|^2 \left\| \begin{bmatrix} \alpha_1 \\ \beta_1 \end{bmatrix} \right\|^2 + \frac{1}{\varepsilon^2} \|\sigma_1\| - \frac{q_1}{\varepsilon^2} \|\sigma_1\| + p_1 \varepsilon \|\xi_1\| \\ & + \frac{2}{\varepsilon} \|\xi_1\| \|\mathbf{P}_1\| \left\| \begin{bmatrix} \alpha_1 \\ \beta_1 \end{bmatrix} \right\| \|\mathbf{v}\|_\infty. \end{aligned}$$

Then, for all $\varepsilon \leq \frac{1}{8\|\mathbf{P}_1\|^2 \left\| \begin{bmatrix} \alpha_1 \\ \beta_1 \end{bmatrix} \right\|^2}$ and all $q_1 \geq 2$, the following holds

$$\dot{V}_1 \leq -\frac{1}{2\varepsilon}\|\xi_1\|^2 - \frac{1}{\varepsilon^2}\sigma + 2\varepsilon\|\xi_1\|(\|\mathbf{P}_1\|\|\mathbf{B}_2\|c_1 + p_1) + \frac{2}{\varepsilon}\|\xi_1\|\|\mathbf{P}_1\| \left\| \begin{bmatrix} \alpha_1 \\ \beta_1 \end{bmatrix} \right\| \|\mathbf{v}\|_\infty \quad (\text{C.5})$$

Finally, for a sufficiently small ε , it is possible to show that $\|\xi_1\|$ will be ultimately bounded by (Theorem 4.5 of [49])

$$\|\xi_1\| \leq k_1 \|\mathbf{v}\|_\infty \quad (\text{C.6})$$

where k_1 is some positive constant.

Now consider the radially unbounded Lyapunov function

$$V_2 = \xi_2^\top \mathbf{P}_2 \xi_2 + \sigma_2 \quad (\text{C.7})$$

where \mathbf{P}_2 is symmetric positive definite matrix such that

$$\mathbf{P}_2 \mathbf{E}_2 + \mathbf{E}_2^\top \mathbf{P}_2 = -\mathbf{I}.$$

The derivative of the Lyapunov function (C.7) satisfies

$$\begin{aligned} \dot{V}_2 \leq & -\frac{1}{\varepsilon} \xi_2^\top \xi_2 + 2\xi_2^\top \mathbf{P}_2 \varepsilon \mathbf{B}_2 (\mathbf{x}_4 - \text{sat}_{r_4}(\eta_3)) + \frac{2}{\varepsilon} \xi_2^\top \mathbf{P}_2 \begin{bmatrix} \alpha_2 \\ \beta_2 \end{bmatrix} \text{sat}_{\sqrt{\sigma_2}}(\text{sat}_{\sqrt{r_2}}(\eta_1) - \hat{\mathbf{x}}_2) \\ & - \frac{q_2}{\varepsilon^2} \sigma_2 + p_2 \varepsilon \|\eta_1 - \hat{\mathbf{x}}_2\| - \frac{2}{\varepsilon} \xi_2^\top \mathbf{P}_2 \begin{bmatrix} \alpha_2 \\ \beta_2 \end{bmatrix} (\mathbf{x}_2 - \text{sat}_{r_2}(\eta_1)). \end{aligned}$$

Again, as the states $\mathbf{x} \in X$ and $\|\text{sat}_{r_4}(\eta_3)\| \leq r_4$ its easy to see that $\|\mathbf{x}_4 - \text{sat}_{r_4}(\eta_3)\| \leq c_2$, where c_2 is a positive constant. Moreover, notice that $\text{sat}_{\sqrt{\sigma_2}}(\text{sat}_{\sqrt{r_2}}(\eta_1) - \hat{\mathbf{x}}_2) \leq \|\sqrt{\sigma_2}\|$, by definition; and, after some time, $\varepsilon \|\mathbf{x}_2 - \text{sat}_{r_2}(\eta_1)\| \leq \|\xi_1\| \leq k_1 \|\mathbf{v}\|_\infty$. Additionally, the following bound holds for some positive value n

$$\|\eta_1 - \hat{\mathbf{x}}_2\| \leq |\eta_1 - \mathbf{x}_2| + |\mathbf{x}_2 - \hat{\mathbf{x}}_2| \leq \frac{\sqrt{n}}{\varepsilon} \|\xi_2\|$$

where $|\cdot|$ is the absolute operator.

Therefore, after some time, the time derivative of V_2 can be upper bounded as

$$\begin{aligned} \dot{V}_2 \leq & -\frac{1}{\varepsilon} \|\xi_2\|^2 + 2\|\xi_2\| \|\mathbf{P}_2\| \varepsilon \|\mathbf{B}_2\| c_2 + 4\|\xi_2\|^2 \|\mathbf{P}_2\|^2 \left\| \begin{bmatrix} \alpha_2 \\ \beta_2 \end{bmatrix} \right\|^2 + \frac{1}{\varepsilon^2} \|\sigma_2\| \\ & - \frac{q_2}{\varepsilon^2} \|\sigma_2\| + p_2 \sqrt{n} \|\xi_2\| + \frac{2}{\varepsilon^2} \|\xi_2\| \|\mathbf{P}_2\| \left\| \begin{bmatrix} \alpha_2 \\ \beta_2 \end{bmatrix} \right\| k_1 \|\mathbf{v}\|_\infty. \end{aligned}$$

Then, for all $\varepsilon \leq \frac{1}{8\|\mathbf{P}_2\|^2 \left\| \begin{bmatrix} \alpha_2 \\ \beta_2 \end{bmatrix} \right\|^2}$ and all $q_2 \geq 2$, the following holds

$$\dot{V}_2 \leq -\frac{1}{2\varepsilon}\|\xi_2\|^2 - \frac{1}{\varepsilon^2}\|\sigma_2\| + 2\|\xi_2\|(\|\mathbf{P}_2\|\varepsilon\|\mathbf{B}_2\|c_2 + p_2\sqrt{n}) + \frac{2}{\varepsilon^2}\|\xi_2\|\|\mathbf{P}_2\| \left\| \begin{bmatrix} \alpha_2 \\ \beta_2 \end{bmatrix} \right\| \|\mathbf{k}_1\|\mathbf{v}\|_\infty$$

Again, for a sufficiently small ε , it is possible to show that $\|\xi_2\|$ will be ultimately bounded by (Theorem 4.5 of [49])

$$\|\xi_2\| \leq \frac{k_1}{\varepsilon}\|\mathbf{v}\|_\infty$$

where k_2 is some positive constant.

Indeed, by repeating this process for all $i = 1, \dots, n$, it is possible to prove that, after some time,

$$\|\xi_i\| \leq \frac{k_i}{\varepsilon^{i-1}}\|\mathbf{v}\|_\infty \quad i = 1, \dots, n. \quad (\text{C.8})$$

Finally, the following bound holds by definition of the coordinate change (B.1)

$$\|\mathbf{x}_i - \hat{\mathbf{x}}_i\| \leq \|\xi_i\|$$

which ends the proof.

Appendix D. PEMFC model parameters

Table 5 summarizes the parameter's value of the model presented in section 3.

References

- [1] IEA, The future of hydrogen, IEA, Paris (2019).
URL <https://www.iea.org/reports/the-future-of-hydrogen>
- [2] M. Jouin, R. Gouriveau, D. Hissel, M.-C. Péra, N. Zerhouni, Degradations analysis and aging modeling for health assessment and prognostics of pemfc, *Reliability Engineering & System Safety* 148 (2016) 78 – 95.
doi:<https://doi.org/10.1016/j.ress.2015.12.003>.
- [3] P. Pei, Q. Chang, T. Tang, A quick evaluating method for automotive fuel cell lifetime, *International Journal of Hydrogen Energy* 33 (14) (2008) 3829 – 3836, tMS07: Symposium on Materials in Clean Power Systems. doi:<https://doi.org/10.1016/j.ijhydene.2008.04.048>.
- [4] X. Li, Principles of fuel cells (2005).
doi:<https://doi.org/10.1002/er.1274>.
- [5] K. Jiao, X. Li, Water transport in polymer electrolyte membrane fuel cells, *Progress in energy and combustion Science* 37 (3) (2011) 221–291.
doi:<https://doi.org/10.1016/j.pecs.2010.06.002>.
- [6] S.-K. Park, S.-Y. Choe, S. ho Choi, Dynamic modeling and analysis of a shell-and-tube type gas-to-gas membrane humidifier for pem fuel cell applications, *International Journal of Hydrogen Energy* 33 (9) (2008) 2273 – 2282. doi:<https://doi.org/10.1016/j.ijhydene.2008.02.058>.

- [7] M. Gerard, J.-P. Poirot-Crouvezier, D. Hissel, M.-C. Pera, Oxygen starvation analysis during air feeding faults in pemfc, *International Journal of Hydrogen Energy* 35 (22) (2010) 12295 – 12307, bio-Ethanol and Other Renewable Sources and Reforming Process for Sustainable Hydrogen Production. doi:<https://doi.org/10.1016/j.ijhydene.2010.08.028>.
- [8] T. Ous, C. Arcoumanis, Degradation aspects of water formation and transport in proton exchange membrane fuel cell: A review, *Journal of Power Sources* 240 (2013) 558 – 582. doi:<https://doi.org/10.1016/j.jpowsour.2013.04.044>.
- [9] Z. Wang, C. Wang, K. Chen, Two-phase flow and transport in the air cathode of proton exchange membrane fuel cells, *Journal of Power Sources* 94 (1) (2001) 40 – 50. doi:[https://doi.org/10.1016/S0378-7753\(00\)00662-5](https://doi.org/10.1016/S0378-7753(00)00662-5).
- [10] U. Pasaogullari, C.-Y. Wang, Two-phase transport and the role of micro-porous layer in polymer electrolyte fuel cells, *Electrochimica Acta* 49 (25) (2004) 4359 – 4369. doi:<https://doi.org/10.1016/j.electacta.2004.04.027>.
- [11] D. A. McKay, J. B. Siegel, W. Ott, A. G. Stefanopoulou, Parameterization and prediction of temporal fuel cell voltage behavior during flooding and drying conditions, *Journal of Power Sources* 178 (1) (2008) 207 – 222. doi:<https://doi.org/10.1016/j.jpowsour.2007.12.031>.

- [12] I. Hussaini, C. Wang, Dynamic water management of polymer electrolyte membrane fuel cells using intermittent rh control, *Journal of Power Sources* 195 (12) (2010) 3822 – 3829. doi:<https://doi.org/10.1016/j.jpowsour.2009.12.112>.
- [13] J. Stumper, S. A. Campbell, D. P. Wilkinson, M. C. Johnson, M. Davis, In-situ methods for the determination of current distributions in pem fuel cells, *Electrochimica Acta* 43 (24) (1998) 3773–3783. doi:[https://doi.org/10.1016/S0013-4686\(98\)00137-6](https://doi.org/10.1016/S0013-4686(98)00137-6).
- [14] A. Geiger, A. Tsukada, E. Lehmann, P. Vontobel, A. Wokaun, G. Scherer, In situ investigation of two-phase flow patterns in flow fields of pefc's using neutron radiography, *Fuel Cells* 2 (2002) 92 – 98. doi:10.1002/fuce.200290007.
- [15] I. Manke, C. Hartnig, M. Grunerbel, W. Lehnert, N. Kardjilov, A. Haibel, A. Hilger, J. Banhart, H. Riesemeier, Investigation of water evolution and transport in fuel cells with high resolution synchrotron x-ray radiograph, *Applied Physics Letters* 90 (2007) 174105. doi:10.1063/1.2731440.
- [16] R. Banerjee, D. Howe, V. Mejjia, S. G. Kandlikar, Experimental validation of two-phase pressure drop multiplier as a diagnostic tool for characterizing pem fuel cell performance, *International Journal of Hydrogen Energy* 39 (31) (2014) 17791 – 17801. doi:<https://doi.org/10.1016/j.ijhydene.2014.08.118>.

- [17] F. Barbir, H. Gorgun, X. Wang, Relationship between pressure drop and cell resistance as a diagnostic tool for pem fuel cells, *Journal of Power Sources* 141 (1) (2005) 96 – 101. doi:<https://doi.org/10.1016/j.jpowsour.2004.08.055>.
- [18] J. Hu, L. Xu, J. Li, C. Fang, S. Cheng, M. Ouyang, P. Hong, Model-based estimation of liquid saturation in cathode gas diffusion layer and current density difference under proton exchange membrane fuel cell flooding, *International Journal of Hydrogen Energy* 40 (41) (2015) 14187 – 14201. doi:<https://doi.org/10.1016/j.ijhydene.2015.09.005>.
- [19] C. Thawornkuno, C. Panjapornpon, Estimation of water content in pem fuel cell, *Chiang Mai Journal of Science* 35 (2008) 212–220.
- [20] X. Zhang, P. Pisu, An unscented kalman filter based on-line diagnostic approach for pem fuel cell flooding, *International Journal of Prognostics and Health Management* 5 (2014).
- [21] J. Luna, E. Usai, A. Husar, M. Serra, Enhancing the efficiency and lifetime of a proton exchange membrane fuel cell using nonlinear model-predictive control with nonlinear observation, *IEEE Transactions on Industrial Electronics* 64 (8) (2017) 6649–6659.
- [22] H. K. Khalil, High-Gain Observers, in: *High-Gain Observers in Nonlinear Feedback Control*, Society of Industrial and Applied Mathematics, Philadelphia, 2017, pp. 17–30.

- [23] A. N. Atassi, H. K. Khalil, A separation principle for the stabilization of a class of nonlinear systems, *IEEE Transactions on Automatic Control* 44 (9) (1999) 1672–1687. doi:10.1109/9.788534.
- [24] A. Teel, L. Praly, Global stabilizability and observability imply semiglobal stabilizability by output feedback, *Systems & Control Letters* 22 (5) (1994) 313 – 325. doi:https://doi.org/10.1016/0167-6911(94)90029-9.
- [25] C. I. Byrnes, A. Isidori, Nonlinear internal models for output regulation, *IEEE Transactions on Automatic Control* 49 (12) (2004) 2244–2247. doi:10.1109/TAC.2004.838492.
- [26] Y. Wu, A. Isidori, R. Lu, H. K. Khalil, Performance recovery of dynamic feedback-linearization methods for multivariable nonlinear systems, *IEEE Transactions on Automatic Control* 65 (4) (2020) 1365–1380. doi:10.1109/TAC.2019.2924176.
- [27] H. Yuan, H. Dai, X. Wei, P. Ming, Model-based observers for internal states estimation and control of proton exchange membrane fuel cell system: A review, *Journal of Power Sources* 468 (2020) 228376. doi:https://doi.org/10.1016/j.jpowsour.2020.228376.
- [28] D. Astolfi, L. Marconi, L. Praly, A. R. Teel, Low-power peaking-free high-gain observers, *Automatica* 98 (2018) 169 – 179. doi:https://doi.org/10.1016/j.automatica.2018.09.009.

- [29] M. Cocetti, S. Tarbouriech, L. Zaccarian, High-gain dead-zone observers for linear and nonlinear plants, *IEEE Control Systems Letters* 3 (2) (2019) 356–361. doi:10.1109/LCSYS.2018.2880931.
- [30] D. Astolfi, A. Alessandri, L. Zaccarian, Stubborn and dead-zone redesign for nonlinear observers and filters, *IEEE Transactions on Automatic Control* 66 (2) (2021) 667–682. doi:10.1109/TAC.2020.2989816.
- [31] J.-P. Gauthier, I. Kupka, *Deterministic observation theory and applications*, Cambridge university press, 2001. doi:https://doi.org/10.1017/cbo9780511546648.
- [32] J. P. Gauthier, H. Hammouri, S. Othman, A simple observer for nonlinear systems applications to bioreactors, *IEEE Transactions on Automatic Control* 37 (6) (1992) 875–880. doi:10.1109/9.256352.
- [33] G. Besancon, A. Ticlea, An immersion-based observer design for rank-observable nonlinear systems, *IEEE Transactions on Automatic Control* 52 (1) (2007) 83–88. doi:10.1109/TAC.2006.889867.
- [34] P. Bernard, *Observer design for nonlinear systems*, Vol. 479, Springer, 2019.
- [35] M. Maggiore, K. M. Passino, A separation principle for a class of non-ucio systems, *IEEE Transactions on Automatic Control* 48 (7) (2003) 1122–1133. doi:10.1109/TAC.2003.814110.

- [36] C. Prieur, S. Tarbouriech, L. Zaccarian, Hybrid high-gain observers without peaking for planar nonlinear systems, in: 2012 IEEE 51st IEEE Conference on Decision and Control (CDC), 2012, pp. 6175–6180. doi:10.1109/CDC.2012.6426449.
- [37] D. Astolfi, L. Praly, Integral action in output feedback for multi-input multi-output nonlinear systems, *IEEE Transactions on Automatic Control* 62 (4) (2017) 1559–1574. doi:10.1109/TAC.2016.2599784.
- [38] A. R. Teel, Further variants of the astolfi/marconi high-gain observer, in: 2016 American Control Conference (ACC), 2016, pp. 993–998. doi:10.1109/ACC.2016.7525044.
- [39] H. K. Khalil, Cascade high-gain observers in output feedback control, *Automatica* 80 (2017) 110 – 118. doi:https://doi.org/10.1016/j.automatica.2017.02.031.
- [40] D. Astolfi, Observers and robust output regulation for nonlinear systems, Ph.D. thesis (2016).
- [41] H. K. Khalil, S. Priess, Analysis of the use of low-pass filters with high-gain observers, *IFAC-PapersOnLine* 49 (18) (2016) 488 – 492, 10th IFAC Symposium on Nonlinear Control Systems NOLCOS 2016. doi:https://doi.org/10.1016/j.ifacol.2016.10.212.
- [42] A. Cecilia, R. Costa-Castelló, High gain observer with dynamic deadzone

- to estimate liquid water saturation in pem fuel cells, *Revista Iberoamericana de Automática e Informática Industrial* 17 (2) (2020) 169–180.
- [43] A. Cecilia, M. Serra, R. Costa-Castelló, Nonlinear adaptive observation of the liquid water saturation in polymer electrolyte membrane fuel cells, *Journal of Power Sources* 492 (2021) 229641. doi:<https://doi.org/10.1016/j.jpowsour.2021.229641>.
- [44] S. Strahl, A. Husar, P. Puleston, J. Riera, Performance improvement by temperature control of an open-cathode PEM fuel cell system, in: *Fuel Cells*, 2014. doi:[10.1002/fuce.201300211](https://doi.org/10.1002/fuce.201300211).
- [45] S. Strahl, R. Costa-Castelló, Model-based analysis for the thermal management of open-cathode proton exchange membrane fuel cell systems concerning efficiency and stability, *Journal of Process Control* 47 (2016) 201 – 212. doi:<https://doi.org/10.1016/j.jprocont.2016.09.004>.
- [46] F. Barbir, *PEM fuel cells: theory and practice*, Academic Press, 2012.
- [47] A. Isidori, Observers with Linear Error Dynamics, in: *Nonlinear Control Systems*, 3rd Edition, Springer-Verlag, London, 1995, pp. 203–217.
- [48] A. Levant, M. Livne, Robust exact filtering differentiators, *European Journal of Control* (2019). doi:<https://doi.org/10.1016/j.ejcon.2019.08.006>.
- [49] H. K. Khalil, J. W. Grizzle, *Nonlinear systems*, Vol. 3, Prentice hall Upper Saddle River, NJ, 2002.